

 Open access • Posted Content • DOI:10.1101/2021.03.30.437779

## **Robust and tunable signal processing in mammalian cells via engineered covalent modification cycles** — [Source link](#)

Ross D. Jones, Yili Qian, Ilia K., Benjamin X. Wang ...+3 more authors





**Institutions:** Massachusetts Institute of Technology

**Published on:** 31 Mar 2021 - bioRxiv (Cold Spring Harbor Laboratory)

**Topics:** Histidine kinase, Signal transduction, Phosphorylation and Response regulator

Related papers:

- [Regulation of Gene Expression and Signaling Pathway Activity in Mammalian Cells by Automated Microfluidics Feedback Control.](#)
- [Inferring the Sign of Kinase-Substrate Interactions by Combining Quantitative Phosphoproteomics with a Literature-Based Mammalian Kinome Network](#)
- [A directed protein interaction network for investigating intracellular signal transduction.](#)
- [Assigning Quantitative Function to Post-Translational Modifications Reveals Multiple Sites of Phosphorylation That Tune Yeast Pheromone Signaling Output](#)
- [DNA origami patterning of synthetic T cell receptors reveals spatial control of the sensitivity and kinetics of signal activation.](#)

Share this paper:    

View more about this paper here: <https://typeset.io/papers/robust-and-tunable-signal-processing-in-mammalian-cells-via-1sn21psp2d>

# Robust and tunable signal processing in mammalian cells via engineered covalent modification cycles

Ross D. Jones<sup>1,2</sup>, Yili Qian<sup>2,3</sup>, Katherine Ilija<sup>1,2</sup>, Benjamin Wang<sup>2,4</sup>, Michael T. Laub<sup>2,4,5</sup>,  
Domitilla Del Vecchio<sup>\*2,3</sup>, and Ron Weiss<sup>\*1,2,6</sup>

<sup>1</sup>Department of Biological Engineering, Massachusetts Institute of Technology, Cambridge, MA, 02139, USA.

<sup>2</sup>Synthetic Biology Center, Massachusetts Institute of Technology, Cambridge, MA, 02139, USA.

<sup>3</sup>Department of Mechanical Engineering, Massachusetts Institute of Technology, Cambridge, MA, 02139, USA.

<sup>4</sup>Department of Biology, Massachusetts Institute of Technology, Cambridge, MA, 02139, USA.

<sup>5</sup>Howard Hughes Medical Institute, Massachusetts Institute of Technology, Cambridge, MA, 02139, USA.

<sup>6</sup>Electrical Engineering and Computer Science Department, Massachusetts Institute of Technology, Cambridge, MA, 02139, USA.

\*Correspondence should be addressed to D.D.V. (ddv@mit.edu). or R.W. (rweiss@mit.edu)

## Abstract

Rewired and synthetic signaling networks can impart cells with new functionalities and enable efforts in engineering cell therapies and directing cell development. However, there is a need for tools to build synthetic signaling networks that are tunable, can precisely regulate target gene expression, and are robust to perturbations within the complex context of mammalian cells. Here, we use proteins derived from bacterial two-component signaling pathways to develop synthetic phosphorylation-based and feedback-controlled devices in mammalian cells with such properties. First, we isolate kinase and phosphatase proteins from the bifunctional histidine kinase EnvZ. We then use these proteins to engineer a synthetic covalent modification cycle, in which the kinase and phosphatase competitively regulate phosphorylation of the cognate response regulator OmpR, enabling analog tuning of OmpR-driven gene expression. Further, we show that the phosphorylation cycle can be extended by connecting phosphatase expression to small molecule and miRNA inputs in the cell, with the latter enabling cell-type specific signaling responses and accurate cell type classification. Finally, we implement a tunable negative feedback controller by co-expressing the kinase-driven output gene with the small molecule-tunable phosphatase. This negative feedback substantially reduces cell-to-cell noise in output expression and mitigates the effects of cell context perturbations due to off-target regulation and resource competition. Our work thus lays the foundation for

establishing tunable, precise, and robust control over cell behavior with synthetic signaling networks.

# 1 Introduction

2 Across all organisms, sensing and processing of environmental factors is critical for growth, proliferation, and  
3 survival<sup>1</sup>. Engineering of mammalian cells to transmute specific intracellular and extracellular inputs into desirable  
4 output behaviors has broad applications in cell therapy, biomanufacturing and the engineering of stem cells, tissues,  
5 and organoids<sup>2-8</sup>. Recently, work has accelerated to rewire natural signaling pathways and engineer synthetic  
6 receptors that sense extracellular inputs<sup>9,10</sup>. A desirable engineered signaling system would have tunable input/output  
7 responses, low output noise, and drive gene expression that is robust to perturbations coming from the extracellular,  
8 cellular, and genetic context of the system<sup>11</sup>. The ability of the signaling system to exhibit such properties depends on  
9 how input signals are processed to generate gene expression outputs. However, relatively little work has been done to  
10 engineer such signal processing behavior in mammalian cells.

11 To date, nearly all engineered signaling systems have utilized either native intracellular signaling domains or  
12 proteolytic mechanisms to transduce extracellular signals into intracellular responses<sup>10</sup>. Interfacing with the cell's  
13 natural signaling networks has been a powerful method to rewire signaling pathways<sup>10</sup>, but it is difficult to modulate  
14 signaling between natural receptors and their gene expression targets due to the complexity of natural signaling  
15 networks in mammalian cells. Alternatively, using proteolysis to liberate gene regulators from the plasma membrane  
16 enables regulation independent from the cell signaling context through non-native proteins such as dCas9 or tTA<sup>10</sup>.  
17 However, since the effector proteins are irreversibly released from the receptor, the ability to tune the input-output  
18 response is limited. Recently, synthetic receptors comprising extracellular receptors or dimerization domains fused to  
19 a bacterial two-component signaling (TCS) protein were shown to successfully transmute ligand inputs to  
20 TCS-regulated transcriptional outputs in mammalian cells<sup>12,13</sup>.

21 The use of TCS proteins in synthetic mammalian signaling networks has the potential for creating tunable, robust  
22 signaling circuits that do not cross-react with existing networks in mammalian cells. TCS pathways are ubiquitous in  
23 bacteria, but are generally rare in eukaryotes and absent in animals<sup>14</sup>. TCS pathways typically comprise a  
24 transmembrane sensor protein called a histidine kinase (HK) and a cognate intracellular effector protein called a  
25 response regulator (RR). In response to specific signal inputs, the HK autophosphorylates on a conserved histidine  
26 residue and then transfers the phosphoryl group to a conserved aspartate residue in the receiver (Rec) domain of the  
27 RR (referred to as the HK's kinase activity). Once phosphorylated, most RRs carry out transcriptional regulation,  
28 though other modes of regulation are possible<sup>15,16</sup>. Unlike typical eukaryotic receptors, in the absence of signal  
29 inputs, most HKs catalyze removal of the phosphoryl group from their cognate RRs (referred to the HK's  
30 phosphatase activity)<sup>16,17</sup>. The presence of signal input alters the conformational state of the HK, thereby tuning its  
31 relative kinase and phosphatase activities<sup>18</sup>. The bifunctional nature of HKs is important for insulating TCS pathways  
32 from off-target interactions<sup>19,20</sup> as well as for increasing the responsiveness to signal inputs<sup>21</sup>. The recently developed

33 TCS-based receptors work by coupling ligand-induced dimerization of the receptor to HK kinase activity and thus  
34 RR-driven gene expression<sup>12,13</sup>. The lack of any known examples of histidine-aspartate phosphorelays in mammalian  
35 cells strongly suggests that these introduced TCS signaling pathways are insulated from mammalian signaling  
36 pathways<sup>12,13,22</sup>.

37 Here, we introduce a framework for engineering signal processing circuits in mammalian cells based on synthetic  
38 covalent modification cycles (CMCs) built with bacterial TCS proteins (Figure 1). In phosphorylation cascades,  
39 phosphatases that are constitutively active or part of a negative feedback loop can impart tunability and robustness to  
40 perturbations into the system through the reversal of substrate phosphorylation<sup>23–27</sup>. To develop such circuits, we  
41 isolate monofunctional kinases and phosphatases from the bifunctional *E. coli* HK EnvZ<sup>28</sup>, then use specific  
42 phosphorylation and dephosphorylation of EnvZ's cognate RR OmpR to regulate downstream gene expression. First,  
43 we illustrate the tunability of this system by using the level of an EnvZ phosphatase to shift the sensitivity of  
44 OmpR-driven gene expression output to the levels of an EnvZ kinase. Further, we show that kinase-to-output dose  
45 responses can be tuned by regulating phosphatase expression with small molecule-inducible degradation domains.  
46 We then build upon this tunability to create novel phosphorylation-based genetic sensors that are capable of cell type  
47 classification and enable cell-type specific signaling responses.

48 A major challenge for developing synthetic genetic circuits is undesirable context-dependence due to factors such  
49 as off-target binding of gene regulators and overloading of cellular factors used in gene expression (*i.e.* resources),  
50 which can perturb gene expression levels<sup>29,30</sup>. Currently, there is a lack of synthetic signaling circuits that are robust  
51 to such context effects in mammalian cells. To address this problem, we introduced robustness to perturbations into  
52 the kinase-to-output process via negative feedback control. The negative feedback is achieved by co-expressing the  
53 output protein with a phosphatase that dephosphorylates OmpR, returning it to an inactive form. The feedback  
54 strength and output level can be tuned via a small molecule-inducible degradation domain fused to the phosphatase.  
55 The addition of feedback control substantially reduces cell-to-cell noise in output expression and mitigates the effects  
56 of off-target translational repression and transcriptional resource loading on the signaling input-output response.  
57 Overall, we present the design and characterization of phosphorylation-regulated genetic modules that will enable  
58 tunable, precise, and robust control of signaling outputs in mammalian cells.

## 59 **2 Results**

### 60 **2.1 Isolation of kinase and phosphatase activity from EnvZ**

61 As a model system for engineering synthetic signal processing circuits, we utilized the well-characterized  
62 EnvZ-OmpR TCS pathway from *E. coli*<sup>31</sup>. Both *in vitro* and *in vivo* in bacteria, it has been shown that the kinase and

63 phosphatase activities of the bifunctional HK EnvZ can be isolated through various mutations<sup>32-34</sup>, truncations<sup>35,36</sup>,  
64 and domain rearrangements<sup>37</sup>. In mammalian cells, it was shown that wild-type (WT) EnvZ is constitutively active<sup>22</sup>,  
65 indicating that it has net-kinase activity, but may still retain some phosphatase activity and thus not operate as  
66 potentially as a pure kinase. To create more monofunctional kinases and phosphatases from EnvZ in mammalian cells,  
67 we generated several variants of EnvZ using established mutations, truncations, domain rearrangements, and novel  
68 combinations thereof (Figure 2 & Supplementary Figure 4).

69 To test for kinase activity, we evaluated the ability of EnvZ variants to activate an OmpR-driven reporter when  
70 transfected into HEK-293FT cells (Supplementary Figure 5). OmpR-activated promoters were made by placing three  
71 to nine OmpR binding sites upstream of a minimal CMV promoter or a synthetic minimal promoter (YB\_TATA<sup>22</sup>,  
72 referred to as minKB), of which the 6xOmpR<sub>BS</sub>-minCMV variant was chosen for use in most downstream  
73 experiments due to its high fold-change in response to OmpR phosphorylation (Supplementary Figure 6). The levels  
74 of OmpR-driven gene expression induced by full-length mutants of EnvZ are shown in Figure 2a. From this initial  
75 screen, we identified two variants, EnvZm2 [T247A] and EnvZm2[AAB], the latter having an extra DHp domain  
76 fused to EnvZ[223+]<sup>37</sup>, that induced higher levels of output expression than WT EnvZ, suggesting that their  
77 phosphatase activity is reduced. Variants expected to be deficient in ATP binding or autophosphorylation based on  
78 previous studies in bacteria were indeed found to lack activation of OmpR-VP64, indicating that in mammalian cells  
79 they also lack kinase activity (Supplementary Figure 5). Moving forward, we used EnvZm2 as our kinase of choice  
80 due to the highly conserved ability of the T247A mutation to reduce or eliminate phosphatase activity in other  
81 HKs<sup>38,39</sup>.

82 To test for phosphatase activity, we co-expressed EnvZm2 with OmpR-VP64 to generate phosphorylated  
83 OmpR-VP64 (P-OmpR-VP64), and then evaluated the ability of our EnvZ variants to deactivate expression of an  
84 OmpR-driven reporter (Supplementary Figure 7). While several EnvZ variants predicted to be phosphatases based on  
85 previous studies indeed showed deactivation of OmpR-driven expression at high concentrations, this deactivation was  
86 comparable to that of a variant predicted to lack any catalytic activity (EnvZm0m1m2m3  
87 [H243A/D244A/T247A/N343K]) (Supplementary Figure 7). Thus, it is possible that these variants were primarily  
88 inhibiting output expression through sequestration of P-OmpR-VP64 from its target promoter, rather than through  
89 dephosphorylation. Indeed, high dosages of such a variant (EnvZm1, [T247A]) can reduce "leaky" activation of  
90 output reporter by non-phosphorylated OmpR-VP64, indicating that the observed reduction in output can occur  
91 absent dephosphorylation (Supplementary Figure 8). Notably, at both low (Supplementary Figure 7) and high  
92 (Supplementary Figure 8) dosages of the variant EnvZ[A] (DHp domain only), we found no apparent phosphatase  
93 activity, contrasting with the original report<sup>36</sup>. Only variant EnvZm1[AAB], having an extra DHp domain fused to  
94 EnvZ[223+] with the mutation [D244A] in both DHp domains, was found to deactivate OmpR-driven expression  
95 more strongly than EnvZm0m1m2m3 (which lacks catalytic activity) (Supplementary Figure 7), suggesting

96 EnvZm1[AAB] has phosphatase activity in mammalian cells. However, at higher dosages of EnvZm1[AAB] and in  
97 the absence of EnvZm2, OmpR-VP64 appears to become activated, indicating that this variant may still retain some  
98 kinase activity (Supplementary Figure 8).

99 Because of the constitutive kinase activity of WT EnvZ and the lack of clear monofunctional phosphatase activity  
100 by purported phosphatase variants of EnvZ, we hypothesized that in mammalian cells, EnvZ may take a structural  
101 conformation that is unfavorable for phosphatase activity. Previously, it was shown that the capability for  
102 autophosphorylation by the HK AgrC can be modulated through changing the rotational state of the DHP domain<sup>40</sup>.  
103 We hypothesized that this rotational conformation may also affect access to the phosphatase state. We therefore  
104 followed the approach of Wang *et al.*<sup>40</sup> to force the alpha helices in the DHP domain of EnvZ into fixed rotational  
105 states using GCN4 leucine zippers (Figure 2c & Supplementary Figure 4). We generated a library of 10  
106 rotationally-locked variants (EnvZt#1-10) with and without a mutation to eliminate ATP binding and hence kinase  
107 activity (m3 – [N343A])<sup>33</sup>. As expected, we observed a range of OmpR-driven gene expression levels that depend on  
108 the putative rotational angle of the DHP domain (Figure 2c). Interestingly, compared to WT EnvZ, all of the EnvZt#  
109 variants yielded equivalent or weaker output activation by OmpR-VP64, while also reducing EnvZm2-induced  
110 expression by at least 3-fold (Figure 2c). Comparing the exact levels of output with and without EnvZm2 in Figure  
111 2c, we found that EnvZt# variants are capable of overriding the initial phosphorylation state of OmpR-VP64 to  
112 ultimately set a defined level of output (Supplementary Figure 9). Most strikingly, all EnvZm3t# variants showed  
113 potent and nearly identical deactivation of OmpR-driven expression back to baseline levels regardless of their  
114 rotational conformation, indicating that all GCN4-fused truncations possess similar phosphatase activities. These  
115 data suggest that the fusion protein itself takes on a conformation that is amenable to phosphatase activity, possibly  
116 due to the formation of a more rigid structure<sup>18</sup>, whilst the rotational state of the DHP domains mostly affects  
117 autophosphorylation.

118 To more quantitatively compare the activation and deactivation of OmpR-driven expression by each of the EnvZ  
119 variants described above, we fit simple first-order models to estimate the dosages of each variant needed for  
120 half-maximal activation or deactivation ( $K_{1/2}$ ) of the output (Supplementary Figure 10). Notably, the EnvZm3t#  
121 variants deactivated output expression with  $K_{1/2}$  values 2- to 3-fold smaller than our previous best putative  
122 phosphatase, EnvZm1[AAB], and 10- to 20-fold smaller than the enzymatically null variant EnvZm0m1m2m3  
123 (Supplementary Figure 10), indicating potent phosphatase activity. Moving forward, we chose to use the variant  
124 EnvZm3t10 as our phosphatase because it has one of the lowest values of  $K_{1/2}$  among all EnvZ variants and  
125 completely deactivates the output down to basal levels (Figure 2 & Supplementary Figure 10).

126 To ensure that the observed putative phosphatase activity is not explained by formation of partially or completely  
127 inactive heterodimers between any putative phosphatases and EnvZm2, we repeated the experiments described above  
128 with CpxA in place of EnvZm2 (Supplementary Figure 11a). CpxA has weak off-target kinase activity for OmpR<sup>20</sup>,

129 and broadly, heterodimerization between different HKs is rare<sup>41</sup>. In the presence of CpxA, the putative phosphatases  
130 similarly, and in some cases more potently, deactivate OmpR-driven expression (Supplementary Figure 11b-c). Thus,  
131 the observed output deactivation is independent of how OmpR-VP64 is phosphorylated.

132 Direct cellular verification of EnvZm3t10 phosphatase activity is challenging due to the acid-lability of  
133 phosphohistidine and phosphoaspartate bonds<sup>42,43</sup> and lack of commercial antibodies against P-OmpR. To verify that  
134 EnvZm3t10 acts as a phosphatase, we thus carried out additional control experiments. Deactivation of OmpR-driven  
135 output by EnvZm3t10 is abolished when adding mutations predicted to eliminate its phosphatase activity, or using  
136 constitutively active variants of OmpR-VP64 (Supplementary Figure 12). Thus, the observed putative phosphatase  
137 activity is not caused by blocking interactions between the kinase and OmpR-VP64, nor by sequestration of  
138 OmpR-VP64. It is thus unlikely that EnvZm3t10 is acting through a mechanism other than direct dephosphorylation  
139 of P-OmpR-VP64.

## 140 **2.2 Tuning kinase-output responses via phosphatase activity**

141 We next constructed a family of tunable genetic devices in which the tunability arises from a CMC between our  
142 preferred kinase (EnvZm2) and phosphatase (EnvZm3t10) acting on OmpR-VP64 (Figure 3a). The inputs to these  
143 devices are the enzymatic activities of the kinase ( $u_K$ ) or phosphatase ( $u_P$ ), or factors that affect such rates. The  
144 device outputs are the transcriptional and translational products driven by OmpR-VP64. To evaluate the tunability of  
145 our engineered CMC, we compared the level of OmpR-VP64-driven output across combinations of kinase and  
146 phosphatase levels, with the phosphatase level regulated at the DNA and protein levels (Figure 3b-d).

147 First, we titrated both kinase and phosphatase levels by dosing in different amounts of plasmid DNA per sample  
148 using poly-transfection<sup>44</sup> (Figure 3b). The 2D input-output map indicates that output expression increases gradually  
149 with the ratio of kinase to phosphatase dosages (Figure 3b, left). As the dosage of phosphatase increases, the amount  
150 of kinase needed to activate the output increases (Figure 3b, center), indicating a decreased sensitivity to kinase input  
151 levels. Likewise, as the level of kinase increases, the amount of phosphatase needed to deactivate the output also  
152 increases (Figure 3b, right). Both results are in accordance with standard models of CMCs<sup>23</sup> (see Supplementary  
153 Note 1 for our derivation).

154 Following the above results, we predicted that we could tune output expression through modulation of  
155 phosphatase stability (Figure 3c). To do so, we fused the phosphatase to small molecule-inducible degradation  
156 domains (DDs) DDd<sup>45</sup> and DDe<sup>46</sup>, which are stabilized by addition of trimethoprim (TMP) and 4-hydroxytamoxifen  
157 (4-OHT), respectively. N-terminal fusions of both DDd and DDe showed the highest fold-changes in output  
158 expression upon addition of the cognate small molecule (Supplementary Figure 13); we chose to move forward with  
159 DDd/TMP for further testing due to lower background signal than DDe/4-OHT. Titration of both the kinase dosage



160 and TMP concentration shows that the output is high only when the kinase is high and TMP is low (Figure 3c, left).  
161 Addition of TMP decreases the sensitivity of the output to kinase (Figure 3c, center) and addition of kinase decreases  
162 the sensitivity of the output to TMP (Figure 3c, right).

163 The response of the TMP-tuned design to kinase and TMP levels depends on the initial level of phosphatase in the  
164 cell. If the level of phosphatase is initially too high, the miRNA cannot suppress it enough to enable output induction  
165 by the kinase; conversely, if the initial level of phosphatase is too low, the kinase dominates the CMC even without  
166 any miRNA added (Supplementary Figure 14). Thus, there is an optimal level of phosphatase at which the ability of  
167 TMP to induce deactivation of gene expression is maximized.

### 168 **2.3 Engineered, cell type-specific signaling responses**

169 In addition to ectopically-expressed factors, endogenous cellular factors can also be plugged in as inputs to the  
170 kinase ( $u_K$ ) and phosphatase ( $u_P$ ) in our engineered CMC, enabling device performance to be tuned based on factors  
171 such as the state of the cell. One particularly useful class of intracellular inputs are miRNAs, which are differentially  
172 expressed across cell types<sup>47</sup> and can be used to identify specific cell states<sup>48</sup>. Building on our CMC, we expected  
173 that miRNAs can be targeted to the mRNAs of the kinase or phosphatase to decrease or increase output expression,  
174 respectively (Figure 4a). An important and difficult challenge in miRNA sensing is to achieve good on/off responses  
175 from the conversion of "high" miRNA inputs into high levels of output expression<sup>44</sup>. We thus investigated our CMC  
176 as a scaffold for improving miRNA input processing and generating cell-type specific signaling responses.

177 As a proof of concept, we built a sensor for a cancer-associated miRNA, miRNA-21-5p (miR-21), which has  
178 previously been used to classify HeLa cells separately from HEK cells<sup>44,48</sup>. To do so, we placed four miR-21 target  
179 sites (T21) in the UTRs of the phosphatase transcription unit (Figure 4b). As a control, we replaced the miR-21 target  
180 sites with four target sites for the synthetic miR-FF4 (TFF4)<sup>49</sup>. In cells expressing miR-21, we expected the  
181 phosphatase to be knocked down, thereby dramatically shifting the balance of the CMC to favor phosphorylation of  
182 OmpR-VP64 and thus activation of the output. Since P-OmpR has only a ~10-30-fold higher affinity for DNA  
183 binding compared to OmpR<sup>50</sup> (which we validated in HEK-293FT cells – Supplementary Figure 17), we included an  
184 endoribonuclease (endoRNase)-based incoherent feedforward loop (iFFL)<sup>51</sup> to constrain cell-to-cell variance in the  
185 expression level of OmpR-VP64 (Supplementary Figure 16). This is helpful due to the high DNA dosage variance of  
186 transfections, within which only a small subset of cells typically receive the ideal dosage of OmpR-VP64, and cells  
187 that receive high DNA dosages are susceptible to spurious activation of output expression by unphosphorylated  
188 OmpR.

189 To test the circuit, we first considered the effect of miR-21 on the kinase-output dose-response curve. We expected  
190 that endogenous expression of miR-21 would selectively sensitize output expression to kinase levels in HeLa cells.

191 Without the phosphatase, the kinase can induce output expression in both HEK and HeLa cells with either circuit  
192 variant (T21 or TFF4), though with stronger output in HeLa cells (Figure 4d, left). When the phosphatase is present  
193 and highly expressed, it suppresses output induction by the kinase in all cases except in HeLa cells with the T21  
194 circuit variant (Figure 4d, right). Note that without the iFFL, the output expression has higher ‘leaky’ background  
195 expression at low ratios of kinase to phosphatase dosages (Supplementary Figures 18 & 19). Depending on the  
196 phosphatase dosage, the T21 variant in HeLa cells has between 10- to 1000-fold higher sensitivity to kinase input  
197 than the TFF4 variant (Supplementary Figure 22). Thus, these results illustrate a novel application of miRNA sensors  
198 for cell-type specific tuning of signaling responses.

199 To optimize our sensor for cell type classification, we followed the approach of Gam *et al.*<sup>44</sup> to systematically  
200 compare the percent of cell positive for output expression at different ratios of each circuit component using  
201 poly-transfection. In our previous classifier designs, a transcriptional repressor such as LacI<sup>48</sup> or BM3R1<sup>44</sup> is  
202 repressed by the miRNA, thereby de-repressing output transcription. Poly-transfection analysis showed that miRNA  
203 sensing in this system is optimized at a particular expression level of repressor that is not too high to prevent  
204 de-repression and not too low to prevent repression in the first place, making optimization difficult<sup>44</sup>. In our current  
205 design, miRNA sensing is instead optimized by the ratio of kinase to phosphatase activity, which is a more flexible  
206 and easily tuned quantity.

207 We found that a 1:1:0.5 ratio of Kinase:Phosphatase:Output plasmids (the latter of which was co-delivered with  
208 the CasE/OmpR-VP64 iFFL) maximized classification accuracy for the T21 vs TFF4 variants in HeLa cells  
209 (Supplementary Figure 20). At this ratio, we obtained a significant ~50% increase in cells positive for output reporter  
210 between the circuit variants in HeLa cells and a ~55% increase between HeLa and HEK-293 for the T21 variant ( $p =$   
211  $0.0017$  and  $0.0056$  respectively, paired two-tailed Student’s T-test – Figure 4d). The area under the curve (AUC) of  
212 the receiver operating characteristic (ROC) curve of the circuit was  $0.83 \pm 0.01$  when comparing T21 vs TFF4  
213 variants in HeLa cells and  $0.93 \pm 0.01$  when comparing the T21 variant in HEK-293 vs HeLa cells (Supplementary  
214 Figure 20). Examining various combinations of dosages of the kinase, phosphatase, and output reporter, we found  
215 that the AUC of the resulting ROC-like curve of our phosphorylation-based classifier ( $0.93 \pm 0.04$  – Supplementary  
216 Figure 21) is higher than that of our recently-optimized transcriptional repressor-based classifier ( $0.84$  – see SI Fig.  
217 16 in Gam *et al.*<sup>44</sup>) for discriminating HEK vs HeLa cells, indicating improved overall performance for cell-type  
218 classification. Thus, the CMC can be used for robust miRNA input processing with minimal tuning effort through  
219 finding the optimal ratio of kinase to phosphatase activities.

## 2.4 Design of a phosphorylation-based feedback controller

The response of expressed genes to their extracellular (or intracellular) inputs are often stochastic and thus imprecise across individual cells<sup>52,53</sup>. In addition, the intracellular context affects the level of gene expression induced by signaling<sup>29,30</sup>, due to factors such as off-target interactions<sup>54</sup> or resource competition<sup>51,55,56</sup> among engineered genes. To remedy these issues and enable construction of signaling circuits that enforce precise and robust signaling responses across cells, we applied feedback control to our CMC (Figure 5a). In both natural<sup>57</sup> and synthetic<sup>58</sup> systems, feedback control can reduce cell-to-cell variance of gene expression in response to signal inputs. Negative feedback has also been used to make gene expression robust to perturbations that affect processes within the feedback loop<sup>59-61</sup>. An advantage of our controller design is that it can be applied without modifying any promoters or intermediate RNA or protein species in the pathway (*e.g.* via the generation of fusions), and simply requires a modification of the output mRNA.

In our controller, the phosphatase is co-expressed with the output gene via a 2A linker<sup>62</sup> and suppresses its own production via dephosphorylation of P-OmpR-VP64 (Figure 5b). Feedback strength can be tuned through TMP regulation of the DDD-fused phosphatase. The level of output set by the controller arises from competitive phosphoregulation of OmpR-VP64 by the kinase and feedback phosphatase. In an ideal system operating with both enzymes saturated, the concentrations of the phosphatase and the output species become insensitive to disturbances affecting their gene expression processes (see Model Box). As TMP selectively regulates phosphatase but not output stability, it can be used as an input to the controller to tune the strength of the feedback. Under the ideal conditions presented above and as long as OmpR-VP64 has not saturated the output promoter, the relationship between the levels of kinase and output is independent of both the exact mechanism by which OmpR-VP64 activates output expression as well as of any perturbations in the transcription and translation processes of the output/phosphatase (see Model Box).

To evaluate the performance of the feedback controller, we first measured the kinase-output responses for open loop (OL) and closed loop (CL) variants. The OL system was made by replacing the phosphatase with Fluc2, which has no effect on OmpR phosphorylation (Figure 2b-c). Since the presence of negative feedback reduces the level of output expression for a given input level of kinase, we tested several OL variants in which the amount of output reporter in transfections was reduced by 3x, 9x, 27x, or 81x (respectively referred to as Fluc2/3, Fluc2/9, Fluc2/27, and Fluc2/81). We define kinase responsiveness as maximal output fold-change in the presence versus absence of kinase. The kinase responsiveness of the OL systems varies from ~10- to ~55-fold. For the CL system variant without DDD fused to the phosphatase, the kinase responsiveness is ~3.5-fold (Figure 5c, left – see Supplementary Figures 23-26 for full poly-transfection scheme and data). Adding DDD to the phosphatase increases the CL kinase responsiveness to ~7.6-fold without TMP, and 6.4-fold for the lowest non-zero amount of TMP that we tested: 0.001

252  $\mu\text{M}$  (Figure 5c, right). The kinase responsiveness of the CL system decreases as more TMP is added (and thus the  
253 phosphatase is stabilized) to the point of approximately matching that of the non-DDd CL system (Figure 5c, right).  
254 The maximum output level of the DDd CL system is up to 10-fold higher than that of the non-DDd CL system and  
255 within  $\sim 5$ -fold of that of the OL system. Thus, tuning the feedback strength via TMP allows the CL system to  
256 recover approximately one third of the dynamic range of the OL system.

257 In the absence of kinase input, we see similar levels of noise in output expression for all OL and CL variants;  
258 however, as the dosage of kinase is increased, we observe a decrease in noise for CL variants and an increase in noise  
259 for OL variants (Figure 5d). At high dosages of kinase, the output noise for OL devices decreases again, but does not  
260 reach the low noise achieved in CL devices. The higher noise in OL systems can be attributed to a more digital-like  
261 transition in output expression per cell as the kinase dosage increases, whereas in CL systems we observe a smooth,  
262 unimodal shift in output expression per cell (Figure 5e, see Supplementary Figure 27 for all variants). The decrease  
263 in noise in CL expression as a function of increasing kinase can likely be attributed to the increasing concentration of  
264 P-OmpR-VP64 on which the phosphatase can actuate negative feedback. Interestingly, tuning feedback strength with  
265 TMP appears to have little effect on the magnitude of output noise observed (Supplementary Figure 28), suggesting  
266 that the faster degradation of the phosphatase did not push our system into a regime where the negative feedback is  
267 significantly attenuated.

268 Comparing the noise as a function of output level for all CL and OL variants, we can see that the noise in the OL  
269 systems peaks at intermediate absolute levels of output (regardless of the kinase dosage needed to achieve such an  
270 output level for a given OL variant), whereas the noise in the CL systems decreases as the output increases due to the  
271 factors described above (Figure 5f). The pattern of noise in the OL variants can potentially be explained by stochastic  
272 transcriptional variation among cells when the output promoter is not saturated. Through negative feedback, the CL  
273 system is likely able to suppress this source of noise.

## 274 **2.5 Robustness to perturbations via feedback control**

275 According to our mathematical modeling comparing the OL and CL circuits, the presence of negative feedback is  
276 expected to impart robustness to perturbations that affect expression of the output protein (see Model Box). We  
277 analyzed robustness in terms of both fold-changes in gene expression resulting from the perturbations and a  
278 robustness score (100% minus the percent deviation from the unperturbed level); a high degree of robustness is  
279 indicated by small absolute fold-changes and high robustness scores. We tested the capability of the CL system to  
280 impart robustness of output expression levels to perturbations that model off-target regulation and resource loading  
281 (Figure 6a). To model off-target regulation by an endogenously- or ectopically-expressed gene regulator such as a  
282 miRNA, we expressed miR-FF4, which binds and cleaves a target site (TFF4) placed in the 3' UTR of the

283 output/phosphatase mRNA, thereby causing mRNA degradation. To model resource loading, we expressed  
284 Gal4-VPR, which strongly sequesters transcriptional resources, such as those recruited by the VP64 activation  
285 domain fused to OmpR, thereby reducing transcription of other genes<sup>51</sup>. In addition to the modeled effects, these  
286 perturbations are useful because they affect output production both before (Gal4-VPR) and after (miR-FF4)  
287 transcription, enabling comparison of the CL system's ability to respond to perturbations at different stages of gene  
288 expression.

289 As expected, we found that the CL system is indeed more robust to miR-FF4 and Gal4-VPR perturbations than  
290 comparable OL variants (Figure 6b-e). Detailed comparisons of the response of all OL and CL variants to both  
291 perturbations are provided in Supplementary Figures 29 & 30. For illustration, we highlight and compare two OL and  
292 two CL variants with similar basal output levels in the absence of kinase (Fluc2, Fluc2/3, EnvZm3t10,  
293 Dd-EnvZm3t10 + 0.001  $\mu$ M TMP – Figure 6b). Without kinase, there is little difference between the effects of  
294 miR-FF4 and Gal4-VPR on the OL and CL systems (Figure 6c, left panels), consistent with the expected lack of  
295 feedback actuation in the absence of P-OmpR-VP64 and our earlier findings of similar levels of noise in the same  
296 regime (Figure 5d). At higher kinase input levels, the fold-changes in output expression for the CL variants in  
297 response to both perturbations are substantially less than those of the OL variants (Figure 6c, right panels).

298 The relative decrease in fold-changes as a function of kinase input dosage is plotted in Figure 6d for two levels of  
299 miR-FF4 and Gal4-VPR perturbations that knock down the OL systems to similar degrees. At medium-to-high  
300 kinase input levels, the feedback controller can respond to the perturbations by sustaining the output level to within  
301 2-4-fold of the nominal (unperturbed) levels, improving significantly over the 6-10-fold changes observed in the OL  
302 systems. The relatively weaker output suppression by Gal4-VPR for both the OL and CL variants at low kinase  
303 dosages may result from generally weaker effects of transcriptional resource sequestration on basal transcription vs  
304 activated transcription<sup>63</sup>. This may offset the general increased susceptibility of the CL system to perturbations in the  
305 low-kinase regime, causing the CL systems to be more evenly perturbed by Gal4-VPR across kinase dosages.

306 Because negative feedback reduces output expression, and since both miR-FF4 and Gal4-VPR knock down gene  
307 expression, a full comparison of the effects of these perturbations on the OL and CL systems must account for  
308 differences in the nominal output expression level. This is because lower nominal output levels can have a reduced  
309 measurable dynamic range of knockdown due to detection limits imposed by the autofluorescence background. To  
310 account for varying nominal output levels for OL and CL systems at different kinase input levels, we compared the  
311 nominal output level versus robustness score for each device. Collating all CL and OL variants at the same miR-FF4  
312 and Gal4-VPR dosages as in Figure 6d, we can see that the CL systems are nearly always more robust than the OL  
313 systems for a given nominal output level (Figure 6e). The only substantial overlap in the plots between the OL and  
314 CL systems occurs at low kinase inputs to the CL system. Quantitatively, for a given nominal output level, we see a  
315 20-30 percentage point increase in robustness score for the CL systems compared to the OL variants. Comparisons

316 across additional dosages of each perturbation show similar results (Supplementary Figures 31 & 32). Thus, our  
 317 phosphorylation-based feedback controller is capable of reducing the impact of perturbations on expression of the  
 318 output gene at both the transcriptional and post-transcriptional levels. Coupled with the reduction in noise (Figure 5),  
 319 these data indicate that the feedback controller can successfully impart precise, tunable, and robust control over gene  
 320 expression in mammalian cells.

### 321 **3 Model Box**

Here we develop a mathematical model to show that covalent modification cycle (CMC)-mediated feedback enables the expression level of a regulated gene to be robust to disturbances. In particular, for a fixed kinase level ( $K_t$ ), we treat the genetic circuit shown in Figure 6 as feedback interconnection of two dynamical processes with input/output (I/O): an engineered CMC that takes phosphatase concentration ( $P_t$ ) as input and outputs P-OmpR-VP64 concentration ( $X^*$ ), and a gene expression process that takes  $X^*$  as input to produce the phosphatase  $P_t$  as output. We use a standard Goldbeter-Koshland model<sup>23</sup> for the dynamics of the CMC:

$$\frac{d}{dt}X^* = \theta_k \frac{(X_t - X^*)K_t}{(X_t - X^*) + K_{M,k}} - \theta_p \frac{X^*P_t}{X^* + K_{M,p}}, \quad (1)$$

where  $\theta_k$  and  $\theta_p$  are catalytic rate constants of the kinase and the phosphatase, respectively,  $K_{M,k}$  and  $K_{M,p}$  are their respective Michaelis-Menten constants, and  $X_t$  is the total amount of OmpR-VP64 (*i.e.*, OmpR-VP and P-OmpR-VP). The expression of  $P_t$  is regulated by an OmpR-activated promoter, which gives rise to the following dynamics:

$$\frac{d}{dt}P_t = \alpha(1 - w)\phi(X^*) - \gamma P_t, \quad (2)$$

where  $\alpha$  is the production rate of  $P_t$  that lumps the rate constants for transcription, translation, and mRNA decay,  $\phi(\cdot)$  is a Hill function satisfying  $\phi' > 0$  for all  $X^*$ ,  $\gamma$  is the protein decay rate constant, and  $0 \leq w < 1$  is a disturbance that models the fold change in production rate of  $P_t$ , which could either arise from indirect transcriptional repression via resource loading or from direct post-transcriptional repression via miRNA (see Figure 6). The output from this feedback-regulated gene is  $Y = \rho P_t$ , since the output protein and phosphatase are co-transcribed but produced as separate proteins using a 2A-linker. We find that the relative sensitivity of output to disturbance  $w$  for this closed-loop system (1)-(2) at a given output level  $Y$  is

$$\mathcal{S}_{CL}(Y) = \frac{1}{Y} \cdot \left| \frac{dY}{dw} \right| = \frac{1}{1-w} \left[ 1 + \frac{\alpha}{\gamma} (1-w) \left| \frac{d}{dY}(\phi \circ h) \right| \right]^{-1}. \quad (3)$$

322 where  $h$  is the transfer curve of the CMC. In comparison, when the CMC in (1) is not connected with (2), the relative  
 323 sensitivity of  $y$  to disturbance  $w$  for the open-loop system (2) is  $\mathcal{S}_{OL} = \frac{1}{1-w}$ . Hence, we have  $\mathcal{S}_{CL} < \mathcal{S}_{OL}$  for all  $y$   
 324 regardless of where the sensitivity is evaluated. This implies that the closed-loop system is always more robust than

325 the open-loop system to disturbance  $w$ . To enable near-perfect adaptation to  $w$ , it is sufficient to increase  
326  $T := \left| \frac{d}{dy}(\phi \circ h) \right| = |h' \cdot \phi'|$ . In particular, if  $T \rightarrow \infty$ , then  $\mathcal{S}_{\text{CL}} \rightarrow 0$ , implying that the closed-loop system can perfectly  
327 adapt to  $w$ . Specifically, for any fixed  $X^*$  and  $y$ , there exists sufficiently small  $K_{M,p}$  and sufficiently large  $X_t$  to make  
328  $|h'|$  arbitrarily large. On the other hand, to ensure  $T$  is large,  $|\phi'|$  must not be too small. This requires us to design the  
329 system so that the OmpR-activated promoter is not saturated. Hence, the  $K_D$  of binding between phosphorylated  
330 OmpR and its target promoter must not be too small<sup>27</sup>. Promoter saturation limits the ability of the output to respond  
331 to changes in OmpR phosphorylation, and thus can limit the benefit of the negative feedback to achieve robustness to  
332 perturbations. Under the ideal operating conditions described above, both enzymes are saturated by their substrates,  
333 which is possible for a small  $K_{M,p}$  and large  $X_t$ . Specifically, if  $K_{M,p} \ll X^*$  and  $X_t \gg K_{M,k}$ , equation (1) can be  
334 approximated by  $dX^*/dt = \theta_k K_t - \theta_p Y/\rho$ , leading to quasi-integral feedback control<sup>27</sup>.

## 335 4 Discussion

336 Here, we developed tunable and precise signaling circuits in mammalian cells that are robust to perturbations  
337 using engineered CMCs derived from bacterial two-component signaling (TCS) proteins (Figure 1). We first  
338 screened engineered variants of the *E. coli* histidine kinase (HK) EnvZ to isolate kinase and phosphatase activity  
339 from this bifunctional protein (Figure 2). We demonstrated tunability in kinase-induced gene expression responses  
340 conferred by small molecule-inducible expression of a phosphatase (Figure 3). Building upon this tunability, we  
341 showed that incorporating target sites for endogenous miRNAs can be used to create cell type-specific signaling  
342 responses through knockdown of phosphatase expression. Co-expressing the phosphatase with the output, we created  
343 a tunable negative feedback loop that reduces both cell-to-cell variation and sensitivity to perturbations of  
344 kinase-induced gene expression (Figure 5 & 6).

345 Combined with recent advances in utilizing TCS proteins to engineer synthetic receptors in mammalian cells<sup>12,13</sup>  
346 and to rewire the specificity of response regulators (RRs) in bacteria<sup>64</sup>, our platform will enable construction of  
347 sophisticated synthetic signaling systems that can connect intracellular and extracellular inputs to diverse target  
348 output in mammalian cells. While much work has so far focused on synthetic receptor engineering<sup>10</sup>, incorporation  
349 of downstream signal processing moieties to improve signaling pathway function has only recently begun to be  
350 explored<sup>65</sup>. In particular, the ability to easily tune signaling pathway activity through phosphatase expression and the  
351 ability to robustly control downstream gene expression processes will facilitate the creation of synthetic signaling  
352 systems that can operate across diverse cellular contexts. In the future, our circuits can form the basis for advanced  
353 cellular computing<sup>66</sup> and feedback control<sup>67</sup> architectures. In addition, connecting signaling pathway activity to  
354 endogenous gene regulation, such as through miRNA regulation of pathway components, will facilitate applications  
355 in guiding differentiation or programming custom signaling for different cellular states.

356 The high degree of orthogonality among existing TCS pathways<sup>68–70</sup> and the relative ease of finding new  
357 orthogonal HK/RR pairs<sup>71</sup> indicates that TCS pathways will be a bountiful source of orthogonal signaling pathways  
358 for use in mammalian cells. To support this effort, we identified several HK-RR pairs that show good orthogonality in  
359 mammalian cells (Supplementary Figure 1-3). Though TCS pathways are absent in animals<sup>14</sup>, histidine and aspartate  
360 phosphorylation is more prevalent than previously thought<sup>43</sup>. The lack of observed histidine to aspartate  
361 phosphotransfer in animals indicates a strong likelihood of orthogonality between TCS pathways and existing  
362 signaling networks in animal cells, though future work will be needed to examine possible cross-talk.

363 Through the implementation of feedback control via CMCs, we have opened the door to creating increasingly  
364 precise and robust responses in engineered signaling pathways. Reducing cell-to-cell variation in signaling output  
365 can be critical for ensuring that cells in a population make uniform, rather than multi-modal or stochastic, decisions.  
366 Reducing sensitivity of output expression to perturbations will help further control individual cellular  
367 decision-making and ensure that engineered signaling systems can operate across diverse cell types and states<sup>51</sup>. In  
368 the future, it may be possible to further improve the robustness to perturbations conferred by our feedback controller.  
369 To achieve near-perfect adaptation to perturbations, the system parameters need to be tuned such that it can operate as  
370 a quasi-integral feedback controller<sup>27,72</sup>. We identified that the  $K_M$  of the phosphatase is likely similar to or higher  
371 than the  $K_D$  of P-OmpR, reducing the efficacy of the feedback (see Model Box). Increasing  $\frac{K_D}{K_M}$  helps ensure that the  
372 phosphatase is saturated with P-OmpR while the output promoter is not, both of which are critical conditions for the  
373 feedback to work in a quasi-integral manner<sup>27</sup> (see Model Box). Further discussion of possible future approaches to  
374 achieve quasi-integral feedback control with our system are discussed in Supplementary Note 2.

375 In natural systems, feedback control plays a critical role in regulating signaling pathway activities. Both negative  
376 and positive feedback are common in TCS pathways<sup>73</sup>. As with the robustness to perturbations conferred by our  
377 feedback controller, negative feedback in natural and engineered TCS pathways in bacteria also allows for adaptation  
378 to signal inputs<sup>25,68,73,74</sup>. A conceptually similar controller to our design is found in bacterial chemotaxis, in which  
379 feedback control via reversible methylation of the receptor protein Tar enables near-perfect adaptation of flagellar  
380 motion to chemoattractants<sup>72,75</sup>. Another close analog can be found in the human ERK1/2 MAPK (mitogen-activated  
381 protein kinase) pathway<sup>76</sup>. In this pathway, Mek is analogous to our HK kinase, Erk is analogous to OmpR-VP64  
382 (though Erk itself only indirectly activates transcription through its targets<sup>77,78</sup>), and the Erk-induced phosphatases  
383 DUSP5/6 are analogous to our HK phosphatase<sup>76,79</sup>. It has been observed that the expression levels of DUSP5/6 are  
384 unaffected by ERK1/2 knockdown<sup>80</sup>, which we propose may result from adaptation of DUSP5/6 levels to ERK1/2  
385 levels due to the negative feedback loop. Negative feedback in both natural and engineered systems, including the  
386 ERK1/2 MAPK pathway, has been shown to convert digital, multimodal input-output responses to more graded,  
387 linear, and uniform responses<sup>57,58,81</sup>. Likewise, our feedback controller is capable of imparting graded, uniform  
388 activation of gene expression in the cell population. Overall, these examples highlight how feedback control plays an



389 important role in the functions of natural systems and will thus serve as a key building block for future synthetic  
390 signaling pathways.

391 In addition to feedback control, natural signaling pathways also incorporate constitutive phosphatase and  
392 regulators thereof to tune signaling functions across diverse cell types. For example, signaling through the T cell  
393 receptor (TCR) is regulated by several inhibitory receptors such as CD45 and phosphatases such as PTPN22, which  
394 suppress TCR pathway activation unless sufficiently high stimulus is encountered<sup>82</sup>. In developing thymocytes,  
395 miR-181a-5p suppresses expression of PTPN22, thereby allowing for TCR pathway stimulation at lower antigen  
396 affinities, providing critical signals for survival and development towards mature T cells<sup>83,84</sup>. In mature T cells, a  
397 variety of miRNAs regulate TCR signaling, other signaling pathways, the cell cycle, and secretion, thereby tuning the  
398 immunological responses of T cells to their environments<sup>85</sup>. Thus, tunable phosphatases and miRNA-regulated  
399 signaling responses similar to the ones we developed can be powerful tools for achieving stage-specific control of  
400 differentiation and tuning cell behavior in different contexts. Future designs may also incorporate miRNAs that  
401 regulate kinase expression to provide an additional layer of tunability, for example by miRNAs that are lower in cell  
402 types or states where higher signaling strengths are desired.

403 As synthetic biology progresses, the development of artificial signaling pathways that reflect natural pathways  
404 through incorporation of multiples layers of negative feedback and tuning will facilitate increasingly sophisticated  
405 and robust control of cellular behavior. The customizable signaling responses enabled through platforms such as ours  
406 may be combined with engineered receptors<sup>12,13</sup> and modular effectors<sup>64</sup> to engineer signaling pathways that  
407 transmute extracellular inputs to various intracellular functions in mammalian cells. Such engineered signaling  
408 pathways will enable precise cell-cell communication and environmental sensing, with applications in engineering  
409 cell therapies, scaling up bioproduction, and programming development of stem cells into specific cells, tissues, and  
410 organoids.

## 411 **5 Methods**

### 412 **Modular plasmid cloning scheme**

413 Plasmids were constructed using a modular Golden Gate strategy similar to previous work in our lab<sup>44,86</sup>. Briefly,  
414 basic parts ("Level 0s" [pL0s] – insulators, promoters, 5'UTRs, coding sequences, 3'UTRs, and terminators) were  
415 created via standard cloning techniques. Typically, pL0s were generated via PCR (Q5 and OneTaq hot-start  
416 polymerases, New England BioLabs (NEB)) followed by In-Fusion (Takara Bio) or direct synthesis of shorter inserts  
417 followed by ligation into pL0 backbones. Oligonucleotides were synthesized by Integrated DNA Technologies (IDT)  
418 or SGI-DNA. pL0s were assembled into transcription units (TUs – "Level 1s" [pL1s]) using BsaI Golden Gate  
419 reactions (10-50 cycles between 16degC and 37degC, T4 DNA ligase). TUs were assembled into multi-TU plasmids

420 ("Level 2s" [pL2s]) using SapI Golden Gate reactions. All restriction enzymes and T4 ligase were obtained from  
421 NEB. Plasmids were transformed into Stellar *E. coli* competent cells (Takara Bio). Transformed Stellar cells were  
422 plated on LB agar (VWR) and propagated in TB media (Sigma-Aldrich). Carbenicillin (100  $\mu\text{g}/\text{mL}$ ), kanamycin (50  
423  $\mu\text{g}/\text{mL}$ ), and/or spectinomycin (100  $\mu\text{g}/\text{mL}$ ) were added to the plates or media in accordance with the resistance  
424 gene(s) on each plasmid. All plasmids were extracted from cells with QIAprep Spin Miniprep and QIAGEN Plasmid  
425 Plus Midiprep Kits. Plasmid sequences were verified by Sanger sequencing at Quintara Biosciences. Genbank files  
426 for each plasmid and vector backbone used in this study are provided in Supplementary Data. Plasmid sequences  
427 were created and annotated using Geneious (Biomatters).

428 In addition to the above, we devised a new scheme for engineering synthetic promoters using what we call "Level  
429 Sub-0" (pSub0) plasmids. The approach for creating promoters from pSub0 vectors is illustrated in Figure 33. In this  
430 system, promoters are divided into up to 10 pSub0 fragments. Because the core elements of a promoter are typically  
431 at the 3' end, we made the pSub0 position vectors start with the 3'-most element and move towards the 5' of the  
432 promoter. Promoter position 1 (pP1) contains the transcription start site (TSS), the +1 position for transcription  
433 initiation, and surrounding sequences. pP1 can also optionally contain transcriptional repressor binding sites (not  
434 done in this study). pP2 contains the TATA box and other upstream core promoter elements<sup>87-89</sup> as desired. Many of  
435 the pP1 and pP2 sequences were derived from the minimal promoters studied by Ede *et al.*<sup>90</sup>. Because the spacing  
436 between the TATA box and +1 site are critical<sup>91</sup>, we broke apart each minimal promoter at equivalent positions such  
437 that they can be interchanged. pP1 and pP2 parts were generally created via PCR reactions using the base pSub0  
438 backbone as a template and adding the inserts via primer overhangs and In-Fusion cloning. Positions 3-10 (pP3-10)  
439 are 'enhancer' positions, wherein we generally encode binding sites (*i.e.* response elements) for transcriptional  
440 activators (such as the RRs in this study), or enhancers from constitutive promoters (not done in this study). pP3-10  
441 plasmids were made by directly ligating annealed primers into pSub0 pP3-10 backbones or through PCR followed by  
442 In-Fusion. The annealed primers were synthesized with 4 bp offsets at each end to naturally create overhangs when  
443 annealed. All pSub0 plasmids include BsaI binding sites in an analogous position to pL0s, such that pSub0s can be  
444 used directly in place of pL0s when generating pL1s (the overhangs are compatible for up to four pSub0 inserts, see  
445 Supplementary Table 1). Because pSub0s and pL0s use BsaI for cloning in the same way, insertion into pL0  
446 backbones using BsaI Golden Gate is inefficient. To more efficiently clone pSub0s into pL0 P.2 (level 0 promoter)  
447 plasmids, we thus generally first performed a Golden Gate reaction with the pSub0s separately from the pL0  
448 backbone, then ligated the Golden Gate product with a pre-fragmented and gel-extracted pL0 backbone.

#### 449 **Cell culture**

450 HEK-293 cells (ATCC), HEK-293FT cells (Thermo Fisher), and HeLa cells (ATCC) were maintained in  
451 Dulbecco's modified Eagle media (DMEM) containing 4.5 g/L glucose, L-glutamine, and sodium pyruvate (Corning)  
452 supplemented with 10% fetal bovine serum (FBS, from VWR). All cell lines used in the study were grown in a

453 humidified incubator at 37deg and 5% CO<sub>2</sub>. All cell lines tested negative for mycoplasma.

#### 454 **Transfections**

455 Cells were cultured to 90% confluency on the day of transfection, trypsinized, and added to new plates  
456 simultaneously with the addition of plasmid-transfection reagent mixtures (reverse transfection). Transfections were  
457 performed in 384-, 96-, 24-, or 6-well pre-treated tissue culture plates (Costar). Following are the volumes, number  
458 of cells, and concentrations of reagents used for 96-well transfections; for 384-, 24- and 6-well transfections, all  
459 values were scaled by a factor of 0.2, 5, or 30, respectively. 120 ng total DNA was diluted into 10  $\mu$ L Opti-MEM  
460 (Gibco) and lightly vortexed. For poly-transfection experiments, the DNA dosage was subdivided equally among  
461 each complex (*e.g.* for two complexes, we delivered 60 ng DNA in each, 40 ng for three complexes, *etc.*) The  
462 transfection reagent was then added and samples were lightly vortexed again. The DNA-reagent mixtures were  
463 incubated for 10-30 minutes while cells were trypsinized and counted. After depositing the transfection mixtures into  
464 appropriate wells, 40,000 HEK-293, 40,000 HEK-293FT, or 10,000 HeLa cells suspended in 100  $\mu$ L media were  
465 added. The reagent used in each experiment along with plasmid quantities per sample and other experimental details  
466 are provided in Supplementary Data. Lipofectamine 3000 was used at a ratio of 2  $\mu$ L P3000 and 2  $\mu$ L Lipo 300 per 1  
467  $\mu$ g DNA. PEI MAX (Polysciences VWR) was used at a ratio of 3  $\mu$ L PEI per 1  $\mu$ g DNA. FuGENE6 (Promega) was  
468 used at a ratio of 3  $\mu$ L FuGENE6 per 1  $\mu$ g DNA. Viafect (Promega) was used at a ratio of 3  $\mu$ L Viafect per 1  $\mu$ g DNA.  
469 The media of the transfected cells was not replaced between transfection and data collection. For all transfections  
470 with TMP (Sigma-Aldrich) or 4-OHT (Sigma-Aldrich), the small molecules were added concurrently with  
471 transfection complexes. In each transfection reagent-DNA complex, we included a hEF1a-driven transfection marker  
472 to indicate the dosage of DNA delivered to each cell.

#### 473 **Luciferase assays and analysis**

474 To measure RR-driven luminescence output in Supplementary Figure 1, we used the Promega Nano-Glo  
475 Dual-Luciferase Reporter Assay System, following the manufacturer's instructions. Briefly, 6,000 HEK-293FT cells  
476 were transfected using the FuGENE6 reagent with 25 ng total DNA comprising the plasmids hPGK:Fluc2  
477 (pGL4.53), an hEF1a-driven HK, an hEF1a-driven RR, an RR-driven promoter expressing NanoLuc, and filler DNA  
478 at 5 ng each. The cells were cultured in 20 uL DMEM supplemented with 10% FBS in 384-well plates with solid  
479 white walls and bottoms (Thermo Fisher) to facilitate luminescence measurements. 48 hours post-transfection, cells  
480 were removed from the incubator and allowed to cool to room temperature. 20  $\mu$ L of ONE-Glo EX Reagent was  
481 added directly to the cultures, and cells were incubated for 3 minutes on an orbital shaker at 900 revolutions per  
482 minute (RPM). Fluc2 signal was measured on a BioTek Synergy H1 hybrid reader, with an integration time of 1 s. 20  
483  $\mu$ L of NanoDLR Stop & Glo Reagent was then added, and cells were again incubated for 3 minutes on an orbital  
484 shaker at 900 RPM. After waiting an additional 10 minutes following shaking, NanoLuc signal was measured on the  
485 same BioTek plate reader, with an integration time of 1 s. NanoLuc signals were normalized by dividing by the Fluc2

486 signals, thereby accounting for differences in transfection efficiency among wells.

#### 487 **Identification of optimal orthogonal TCS pairs**

488 To identify the optimal set of orthogonal TCS interactions, we ran a MATLAB script to score all possible  
489 combinations of 4-7 HK-RR protein pairs. The script uses a scoring function to evaluate each particular subset of  
490 HKs and RRs. The data input into the scoring function is a matrix of output expression levels driven by the RRs in  
491 the presence of the selected HKs. The scoring function first identifies a reference value for each row and column by  
492 iteratively finding the maximum value in the matrix, blocking off the rest of the values in its row and column, then  
493 repeating until each row and column has one reference value. The reference value is then divided by the rest of the  
494 values in its row and column, and the quotients are multiplied together to give a score. The scores for each reference  
495 value are then again multiplied together to get a final score for a particular combination of HKs and RRs. After  
496 iterating through all possible such combinations, the highest final score for a given submatrix size is selected. The  
497 method gave qualitatively orthogonal combinations for up to 7 TCS pairs; we thus present the optimized 7-matrix in  
498 Supplementary Figure 1.

#### 499 **Flow cytometry**

500 To prepare samples in 96-well plates for flow cytometry, the following procedure was followed: media was  
501 aspirated, 50  $\mu$ L PBS (Corning) was added to wash the cells and remove FBS, the PBS was aspirated, and 40  $\mu$ L  
502 Trypsin-EDTA (Corning) was added. The cells were incubated for 5-10 minutes at 37deg C to allow for detachment  
503 and separation. Following incubation, 80  $\mu$ L of DMEM without phenol red (Gibco) with 10% FBS was added to  
504 inactivate the trypsin. Cells were thoroughly mixed to separate and suspend individual cells. The plate(s) were then  
505 spun down at  $400 \times g$  for 4 minutes, and the leftover media was aspirated. Cells were resuspended in 170  $\mu$ L flow  
506 buffer (PBS supplemented with 1% BSA (Thermo Fisher), 5 mM EDTA (VWR), and 0.1% sodium azide  
507 (Sigma-Aldrich) to prevent clumping). For prepping plates of cells with larger surface areas, all volumes were scaled  
508 up in proportion to surface area and samples were transferred to 5 mL polystyrene FACS tubes (Falcon) after  
509 trypsinization. For standard co-transfections, 10,000-50,000 cells were collected per sample. For the  
510 poly-transfection experiment and transfections into cells harboring an existing lentiviral integration, 100,000-200,000  
511 cells were collected per sample.

512 For all experiments, samples were collected on a BD LSR Fortessa equipped with a 405nm laser with 450/50nm  
513 filter ('Pacific Blue') for measuring TagBFP or EBFP2, 488 laser with 530/30 filter ('FITC') for measuring EYFP or  
514 mNeonGreen, 561nm laser with 582/15nm filter ('PE') or 610/20nm filter ('PE-Texas Red') for measuring mKate2 or  
515 mKO2, and 640 laser with 780/60nm filter ('APC-Cy7') for measuring iRFP720. 500-2000 events/s were collected  
516 either in tubes via the collection port or in 96-well plates via the high-throughput sampler (HTS). All events were  
517 recorded and compensation was not applied until processing the data (see below).

#### 518 **Flow cytometry data analysis**

519 Analysis of flow cytometry data was performed using our MATLAB-based flow cytometry analysis pipeline  
520 ([https://github.com/Weiss-Lab/MATLAB\\_Flow\\_Analysis](https://github.com/Weiss-Lab/MATLAB_Flow_Analysis)). Basic processing steps follow the procedures  
521 described previously<sup>51</sup>. In addition, we frequently utilized our new poly-transfection technique and associated  
522 methods<sup>44</sup> to characterize and optimize circuits. Poly-transfection enables rapid and accurate assessment of  
523 dose-response curves for genetic components<sup>44</sup>, such as the kinases and phosphatases in our circuits. Full schematics  
524 describing each poly-transfection experiment are shown in the SI (*e.g.* Supplementary Figure 5a).

525 Multi-dimensional binning of poly-transfection data was performed by first defining bin edges in each dimension  
526 (*i.e.* for the transfection markers for each poly-transfection complex), then assigning each cell to a bin where the  
527 cell's expression of these markers was less-than-or-equal-to the high bin edges and greater-than the low bin edges.  
528 Bins with three or fewer cells were ignored (values set to NaN in the MATLAB code) to avoid skewing by outliers in  
529 sparsely-populated samples (*e.g.* HeLa cells). Such binning is demonstrated via colorization of cells by their bin  
530 assignment in the SI (*e.g.* Supplementary Figure 5b). In order to avoid the artefact of negative fold-changes,  
531 non-positive fluorescence values were discarded prior to making measurements on binned or gated populations. In  
532 the second and third experimental repeats of the miRNA-dependent signaling/classifier data in Figure 4 and  
533 Supplementary Figures 18-22, a newly-prepared Output Marker plasmid was later discovered to have ~8-fold lower  
534 concentration than expected due to a measurement error on the nanodrop. To account for this, the bins for the Output  
535 Marker in those samples are shifted down by 10x (so as to match the same bin boundaries as in the first repeat).

536 To find the optimal ratio of components in the miR-21 sensor for high cell classification accuracy, we scanned  
537 ratios between 1000:1 to 1:1000 of K:P and output plasmid:K/P, roughly halving the ratio between steps. At each  
538 combination of ratios, a trajectory was computed and all cells within 0.25 biexponential units of the trajectory based  
539 on euclidean distance were recorded. Accuracy was computed as described below, and accuracy values were  
540 compared across all ratios for each experimental repeat. From this scanning of trajectories at different ratios of  
541 components, we found that a 1:1:0.5 ratio of K:P:Output plasmid gave the highest accuracy. This optimal trajectory  
542 was used to sub-sample cells for display in Figure 4f & Supplementary Figure 20, finding percent positive for output  
543 in Figure 4g and calculating ROCs/AUCs in Supplementary Figure 20.

544 In the case of simple co-transfections and sub-sampled trajectories, cells were considered to be transfected if they  
545 were positive for the output/transfection marker *or* the output reporter. When computing summary statistics from  
546 binned data, such thresholding is unnecessary since binning already isolates the cell sub-population for measurement.

#### 547 **Calculation of cell classification metrics**

548 Sensitivity was defined as the percent of cells positive for the output reporter in HeLa cells transfected with the  
549 T21 circuit variant. Specificity was defined as 100 minus the percent of cells positive for the output in HeLa cells  
550 with the TFF4 variant or in HEK-293 cells with the T21 variant. The former was considered the more ideal  
551 comparison for evaluating classification performance due to higher overall expression of the circuit in HeLa cells

552 compared to HEKs (Supplementary Figure 18). Accuracy was computed by averaging sensitivity and specificity.

553 ROC curves in Supplementary Figure 20 were generated by scanning thresholds starting at  $-10^8$ , then 0, then  $15$   
554 log-spaced steps between  $10^3$  and  $10^8$ . The AUCs were computed individually for each experimental repeat by  
555 trapezoidal area approximation using the MATLAB function ‘trapz()’  
556 (<https://www.mathworks.com/help/matlab/ref/trapz.html>). The AUC-like curves in Supplementary  
557 Figure 21 were computed by fitting data from each experimental repeat with a bi-normal classification model in  
558 MATLAB (see below for details of the fitting algorithm used).

### 559 **Calculation of p-values**

560 P-values shown in Figure 4 were computed using the MATLAB function ‘ttest()’  
561 (<https://www.mathworks.com/help/stats/ttest.html>). Samples were paired per experimental repeat and  
562 the test was two-tailed.

### 563 **Calculation of fold-changes and robustness scores**

For quantifying the effects of EnvZ variants and perturbations, we measured fold-changes by dividing the median  
output level of each sample by that of the equivalent sample in the absence of the EnvZ variant or perturbation. For  
perturbation experiments, the level of output absent perturbation is referred to as the nominal output level.

$$\text{Fold-}\Delta(\text{Input/perturbation bin}_x) = \frac{\text{Output}(\text{Input/perturbation bin}_x)}{\text{Output}(\text{Input/perturbation bin}_1)} \quad (4a)$$

564 Where  $\log_2$ -transformed fold-changes are shown for experiments with multiple repeats, the values shown are the  
565 mean of the  $\log_2$ -transformed fold-changes, rather than the  $\log_2$ -transformation of the mean of the fold-changes. This  
566 order of operations ensures that standard deviations of the fold-changes can be computed directly on the  
567  $\log_2$ -transformed scale.

We computed robustness scores from the fold-changes using the formulae below:

$$\text{Robustness}(\text{Perturbation bin}_x) = 100 \cdot \left(1 - \left|1 - \text{Fold-}\Delta(\text{Perturbation bin}_x)\right|\right) \quad (5a)$$

### 568 **Quantification of cell-to-cell output variance**

569 To measure noise, we computed the interquartile range (IQR) of the output distributions. As we chose the median  
570 to represent the middle of the distribution, the IQR is a corresponding non-parametric measurement of noise. Since  
571 gene expression noise is approximately log-distributed, we  $\log_10$ -transformed the data prior to computing the IQR.  
572 As with calculations of the medians, negative fluorescent values were discarded when computing the IQR to avoid  
573 artefacts.

### 574 **Model fitting**

575 Where possible, fluorescent reporters were used to estimate the concentration of a molecular species for the  
576 purpose of model fitting.

577 For fitting all models, we used the MATLAB function ‘lsqcurvefit()’  
578 (<https://www.mathworks.com/help/optim/ug/lsqcurvefit.html>), which minimizes the sum of the squares  
579 of the residuals between the model and the data. In general, fits were made with cells subsampled from bins, as  
580 indicated for each figure. In Supplementary Figure 21, the fits were made using the true/false positive rates for each  
581 bin. Fits were always performed individually per experimental repeat, then means and standard deviations were  
582 computed for individual fit parameters.

583 Goodness of fit was measured by computing the normalized root-mean-square error CV(RMSE) using the  
584 following formula:

$$\text{CV(RMSE)} = \frac{\sqrt{\frac{1}{\bar{y}} \sum_i (y(x_i) - f(x_i))^2}}{\bar{y}}$$

585 Where  $y(x_i)$  is the value of the data at the input value  $x_i$ ,  $\bar{y}$  is the mean of  $y$  for all values of  $x$ , and  $f(x_i)$  is the  
586 function output at input value  $x_i$ .

587 Fitting functions:

588 Activation of transcription by OmpR-VP64:

$$y = \alpha_0 + (\alpha - \alpha_0) \frac{x^2}{K_{1/2}^2 + x^2} \quad (6)$$

589 The cooperativity of OmpR was assumed to be two because it forms a dimer once phosphorylated to bind  
590 DNA<sup>15,92</sup>.

591 Activation of OmpR-VP64-driven expression by kinase: (see Supplementary Note 1 for more details):

$$y = \alpha_0 + (\alpha - \alpha_0) \frac{x^2}{K_{1/2}^2 + x^2} \quad (7)$$

592 Deactivation of OmpR-VP64 by phosphatase:

$$y = \alpha_0 + (\alpha - \alpha_0) \frac{K_{1/2}^2}{K_{1/2}^2 + x^2} \quad (8)$$

593 While OmpR-VP64 has not been completely tuned over to P-OmpR-VP64, the amount of P-OmpR-VP64 is  
594 assumed to be proportional to the level of kinase because the production rate is only dependent on the kinase. In the  
595 presence of the phosphatase, the decay rate becomes overwritten by the dephosphorylation reaction. Thus, these  
596 proteins can be plugged directly into the OmpR-VP64 activation function, such that the kinase is proportional to  
597 OmpR and the phosphatase is inversely so. Because of the inversion, the phosphatase function becomes a  
598 repression-form Hill function.

599 The bi-normal fitting function for ROC curves is included with our MATLAB flow cytometry analysis package on  
600 GitHub (‘model\_ROC.mat’). In short, the measurement of the fraction of cells positive for the output reporter is  
601 assumed to follow a normal distribution with  $\mu_1 = 0$  and  $\sigma_1 = 1$  for the negative observations (TFF4 or HEK cells in

602 our case) and a normal distribution with unknown  $\mu_2$  and  $\sigma_2$  for the positive observations (T21 in HeLa cells).  $\mu_2$  and  
603  $\sigma_2$  are fit such that the true positive rate for a given false positive rate approximates that of the data.

## 604 **6 Data Availability**

605 Sequences for all plasmids used in this study are provided as GenBank files in Supplementary Data. New plasmids  
606 used in this study will be available on Addgene upon publication. Raw .fcs files are available from the corresponding  
607 authors upon reasonable request.

## 608 **7 Code Availability**

609 General MATLAB code for use in .fcs file processing and analysis are available under an open-source license in  
610 our GitHub repository at [https://github.com/Weiss-Lab/MATLAB\\_Flow\\_Analysis](https://github.com/Weiss-Lab/MATLAB_Flow_Analysis). Specific .m scripts for  
611 each experiment are available from the corresponding authors upon reasonable request.

## 612 **8 Acknowledgements**

613 We would like to acknowledge Douglas Lauffenburger, Ahmad Khalil, and Conor McClune for helpful discussion.  
614 Thanks to Bre DiAndreth for the MATLAB code to find optimal orthogonal TCS pairs; Jeremy Gam for the  
615 MATLAB code to fit ROC curves and plasmids; both Jin Huh and Kalon Overholt for plasmids and helpful  
616 discussion; and Nika Shakiba, Melody Wu, and Margaret Zhang for help with cloning pSub0 plasmids.

## 617 **9 Author Contributions**

618 R.D.J., Y.Q., D.D.V., and R.W. designed the study; R.W., D.D.V., and M.T.L. secured funding; R.D.J., K.I., and  
619 B.W. performed the experiments; R.D.J. and B.W. analyzed the data; Y.Q. and R.D.J. developed the mathematical  
620 models; R.D.J., Y.Q., D.D.V., and R.W. wrote the manuscript; R.D.J., Y.Q., K.I., B.W., M.T.L., D.D.V., and R.W.  
621 edited and/or reviewed the manuscript.

## 622 **10 Funding**

623 This work was supported by the National Science Foundation (MCB-1840257) and the United States Air Force  
624 Office of Scientific Research (FA9550-14-1-0060).



## 625 **11 Competing Interests Statement**

626 The Massachusetts Institute of Technology has filed a patent application on behalf the inventors (R.D.J., J.H., and  
627 R.W.) of phosphorylation-based miRNA sensor design described (US Provisional Application No. 16/528,772) and a  
628 provisional application on behalf of the inventors (R.D.J., Y.Q., D.D.V., and R.W.) of the phosphorylation-based  
629 feedback controller design described. The remaining authors declare no conflict of interest.

## 630 **References**

- 631 1. Jordan, J. D., Landau, E. M. & Iyengar, R. Signaling networks: The origins of cellular multitasking. *Cell* **103**,  
632 193–200 (2000).
- 633 2. Lipsitz, Y. Y., Timmins, N. E. & Zandstra, P. W. Quality cell therapy manufacturing by design. *Nature*  
634 *Biotechnology* **34**, 393–400 (2016).
- 635 3. Brenner, M. J., Cho, J. H., Wong, N. M. & Wong, W. W. Synthetic Biology: Immunotherapy by Design.  
636 *Annual Review of Biomedical Engineering* **20**, 95–118 (2018).
- 637 4. Kamm, R. D. *et al.* Perspective: The promise of multi-cellular engineered living systems. *APL Bioengineering*  
638 **2**, 040901 (2018).
- 639 5. Rossi, G., Manfrin, A. & Lutolf, M. P. Progress and potential in organoid research. *Nature Reviews Genetics*  
640 **19**, 671–687 (2018).
- 641 6. Tewary, M., Shakiba, N. & Zandstra, P. W. Stem cell bioengineering: building from stem cell biology. *Nature*  
642 *Reviews Genetics* **19**, 595–614 (2018).
- 643 7. Kitada, T., DiAndreth, B., Teague, B. & Weiss, R. Programming gene and engineered-cell therapies with  
644 synthetic biology. *Science* **359**, eaad1067 (Feb. 2018).
- 645 8. Scheller, L. & Fussenegger, M. From synthetic biology to human therapy: engineered mammalian cells.  
646 *Current Opinion in Biotechnology* **58**, 108–116 (2019).
- 647 9. Johnson, M. B., March, A. R. & Morsut, L. Engineering multicellular systems: Using synthetic biology to  
648 control tissue self-organization. *Current Opinion in Biomedical Engineering* **4**, 163–173 (2017).
- 649 10. Kojima, R., Aubel, D. & Fussenegger, M. Building sophisticated sensors of extracellular cues that enable  
650 mammalian cells to work as “doctors” in the body. *Cellular and Molecular Life Sciences* (2020).
- 651 11. Shakiba, N., Jones, R. D., Weiss, R. & Vecchio, D. D. Context-aware synthetic biology by controller design:  
652 engineering the mammalian cell. *Cell Systems* **12**, 561–592 (2021).

- 653 12. Maze, A. & Benenson, Y. Artificial signaling in mammalian cells enabled by prokaryotic two-component  
654 system. *Nature Chemical Biology* **16**, 179–187 (2019).
- 655 13. Scheller, L. *et al.* Phosphoregulated orthogonal signal transduction in mammalian cells. *Nature*  
656 *Communications* **11**, 3085 (2020).
- 657 14. Capra, E. J., Perchuk, B. S., Skerker, J. M. & Laub, M. T. Adaptive mutations that prevent crosstalk enable the  
658 expansion of paralogous signaling protein families. *Cell* **150**, 222–232 (2012).
- 659 15. Galperin, M. Y. Structural classification of bacterial response regulators: Diversity of output domains and  
660 domain combinations. *Journal of Bacteriology* **188**, 4169–4182 (2006).
- 661 16. Gao, R. & Stock, A. M. Biological Insights from Structures of Two-Component Proteins. *Annual Review of*  
662 *Microbiology* **63**, 133–154 (2009).
- 663 17. Huynh, T. N. & Stewart, V. Negative control in two-component signal transduction by transmitter phosphatase  
664 activity. *Molecular Microbiology* **82**, 275–286 (2011).
- 665 18. Jacob-Dubuisson, F., Mechaly, A., Betton, J. M. & Antoine, R. Structural insights into the signalling  
666 mechanisms of two-component systems. *Nature Reviews Microbiology* **16**, 585–593 (2018).
- 667 19. Laub, M. T. & Goulian, M. Specificity in Two-Component Signal Transduction Pathways. *Annual Review of*  
668 *Genetics* **41**, 121–145 (2007).
- 669 20. Siryaporn, A. & Goulian, M. Cross-talk suppression between the CpxA-CpxR and EnvZ-OmpR  
670 two-component systems in *E. coli*. *Molecular Microbiology* **70**, 494–506 (2008).
- 671 21. Yang, Y. & Inouye, M. *Requirement of both kinase and phosphatase activities of an Escherichia coli receptor*  
672 *(Taz1) for ligand-dependent signal transduction* 1993.
- 673 22. Hansen, J. *et al.* Transplantation of prokaryotic two-component signaling pathways into mammalian cells.  
674 *PNAS* **111**, 15705–15710 (2014).
- 675 23. Goldbeter, A. & Koshland, D. E. An amplified sensitivity arising from covalent modification in biological  
676 systems. *PNAS* **78**, 6840–6844 (1981).
- 677 24. Asthagiri, A. R. & Lauffenburger, D. A. A computational study of feedback effects on signal dynamics in a  
678 mitogen-activated protein kinase (MAPK) pathway model. *Biotechnology Progress* **17**, 227–239 (2001).
- 679 25. Chang, Y. C., Armitage, J. P., Papachristodoulou, A. & Wadhams, G. H. A single phosphatase can convert a  
680 robust step response into a graded, tunable or adaptive response. *Microbiology* **159**, 1276–1285 (2013).
- 681 26. Nilgiriwala, K. S., Jiménez, J., Rivera, P. M. & Del Vecchio, D. Synthetic Tunable Amplifying Buffer Circuit  
682 in *E. coli*. *ACS Synthetic Biology* **4**, 577–584 (2015).

- 683 27. Qian, Y. & Del Vecchio, D. Realizing “Integral Control” In Living Cells: How To Overcome Leaky Integration  
684 Due To Dilution? *Journal of The Royal Society Interface* **15**, 20170902 (2018).
- 685 28. Cai, S. J. & Inouye, M. EnvZ-OmpR interaction and osmoregulation in Escherichia coli. *Journal of Biological*  
686 *Chemistry* **277**, 24155–24161 (2002).
- 687 29. Del Vecchio, D. Modularity, context-dependence, and insulation in engineered biological circuits. *Trends in*  
688 *Biotechnology* **33**, 111–119 (2015).
- 689 30. Grunberg, T. W. & Del Vecchio, D. Modular Analysis and Design of Biological Circuits. *Current Opinion in*  
690 *Biotechnology* **63**, 41–47 (2020).
- 691 31. Stock, A. M., Robinson, V. L. & Goudreau, P. N. Two-Component Signal Transduction. *Annual Review of*  
692 *Biochemistry* **69**, 183–215 (2000).
- 693 32. Skarphol, K., Waukau, J. & Forst, S. A. Role of His243 in the phosphatase activity of EnvZ in Escherichia  
694 coli. *Journal of Bacteriology* **179**, 1413–1416 (1997).
- 695 33. Hsing, W., Russo, F. D., Bernd, K. K. & Silhavy, T. J. Mutations that alter the kinase and phosphatase  
696 activities of the two-component sensor EnvZ. *Journal of Bacteriology* **180**, 4538–4546 (1998).
- 697 34. Capra, E. J. *et al.* Systematic dissection and trajectory-scanning mutagenesis of the molecular interface that  
698 ensures specificity of two-component signaling pathways. *PLoS Genetics* **6**, e1001220 (2010).
- 699 35. Park, H. & Inouye, M. Mutational analysis of the linker region of EnvZ, an osmosensor in Escherichia coli.  
700 *Journal of Bacteriology* **179**, 4382–4390 (1997).
- 701 36. Zhu, Y., Qin, L., Yoshida, T. & Inouye, M. Phosphatase activity of histidine kinase EnvZ without kinase  
702 catalytic domain. *PNAS* **97**, 7808–7813 (2000).
- 703 37. Qin, L., Dutta, R., Kurokawa, H., Ikura, M. & Inouye, M. A monomeric histidine kinase derived from EnvZ,  
704 an Echerichia coli osmosensor. *Molecular Microbiology* **36**, 24–32 (2000).
- 705 38. Huynh, T. N., Noriega, C. E. & Stewart, V. Conserved mechanism for sensor phosphatase control of  
706 two-component signaling revealed in the nitrate sensor NarX. *PNAS* **107**, 21140–5 (2010).
- 707 39. Willett, J. W. & Kirby, J. R. Genetic and Biochemical Dissection of a HisKA Domain Identifies Residues  
708 Required Exclusively for Kinase and Phosphatase Activities. *PLoS Genetics* **8**, e1003084 (2012).
- 709 40. Wang, B., Zhao, A., Novick, R. P. & Muir, T. W. Activation and inhibition of the receptor histidine kinase  
710 AgrC occurs through opposite helical transduction motions. *Molecular Cell* **53**, 929–940 (2014).
- 711 41. Ashenberg, O., Rozen-Gagnon, K., Laub, M. T. & Keating, A. E. Determinants of homodimerization  
712 specificity in histidine kinases. *Journal of Molecular Biology* **413**, 222–235 (2011).

- 713 42. Egger, L. a., Park, H. & Inouye, M. Signal transduction via the histidyl-aspartyl phosphorelay. *Genes to Cells*  
714 **2**, 167–184 (1997).
- 715 43. Hardman, G. *et al.* Strong anion exchange-mediated phosphoproteomics reveals extensive human  
716 non-canonical phosphorylation. *The EMBO Journal* **38**, 1–22 (2019).
- 717 44. Gam, J. J., DiAndreth, B., Jones, R. D., Huh, J. & Weiss, R. A 'poly-transfection' method for rapid, one-pot  
718 characterization and optimization of genetic systems. *Nucleic Acids Research* **47**, e106 (2019).
- 719 45. Iwamoto, M., Björklund, T., Lundberg, C., Kirik, D. & Wandless, T. J. A general chemical method to regulate  
720 protein stability in the mammalian central nervous system. *Chemistry and Biology* **17**, 981–988 (2010).
- 721 46. Miyazaki, Y., Imoto, H., Chen, L. & Wandless, T. Destabilizing domains derived from the human estrogen  
722 receptor. *Journal of the American Chemical Society* **134**, 3942–3945 (2012).
- 723 47. Landgraf, P. *et al.* A Mammalian microRNA Expression Atlas Based on Small RNA Library Sequencing. *Cell*  
724 **129**, 1401–1414 (2007).
- 725 48. Xie, Z., Wroblewska, L., Prochazka, L., Weiss, R. & Benenson, Y. Multi-Input RNAi-Based Logic Circuit for  
726 Identification of Specific Cancer Cells. *Science* **333**, 1307–1311 (2011).
- 727 49. Rinaudo, K. *et al.* A universal RNAi-based logic evaluator that operates in mammalian cells. *Nature*  
728 *Biotechnology* **25**, 795–801. arXiv: arXiv:1011.1669v3 (2007).
- 729 50. Head, C. G., Tardy, A. & Kenney, L. J. Relative binding affinities of OmpR and OmpR-phosphate at the ompF  
730 and ompC regulatory sites. *Journal of Molecular Biology* **281**, 857–870 (1998).
- 731 51. Jones, R. D. *et al.* An endoribonuclease-based feedforward controller for decoupling resource-limited genetic  
732 modules in mammalian cells. *Nature Communications*, 5690 (2020).
- 733 52. Raj, A., Peskin, C. S., Tranchina, D., Vargas, D. Y. & Tyagi, S. Stochastic mRNA synthesis in mammalian  
734 cells. *PLoS Biology* **4**, 1707–1719 (2006).
- 735 53. Gutierrez, P. S., Monteoliva, D. & Diambra, L. Cooperative Binding of Transcription Factors Promotes  
736 Bimodal Gene Expression Response. *PLoS ONE* **7** (2012).
- 737 54. Meyer, A. J., Segall-Shapiro, T. H., Glassey, E., Zhang, J. & Voigt, C. A. Escherichia coli “Marionette” strains  
738 with 12 highly optimized small-molecule sensors. *Nature Chemical Biology* **15**, 196–204 (2019).
- 739 55. Qian, Y., Huang, H. H., Jiménez, J. I. & Del Vecchio, D. Resource Competition Shapes the Response of  
740 Genetic Circuits. *ACS Synthetic Biology* **6** (2017).
- 741 56. Frei, T. *et al.* Characterization and mitigation of gene expression burden in mammalian cells. *Nature*  
742 *Communications* **11**, 4641 (2020).

- 743 57. Sturm, O. E. *et al.* The mammalian MAPK/ERK pathway exhibits properties of a negative feedback amplifier.  
744 *Science Signaling* **3**, ra90 (2010).
- 745 58. Nevozhay, D., Adams, R. M., Murphy, K. F., Josic, K. & Balazsi, G. Negative autoregulation linearizes the  
746 dose-response and suppresses the heterogeneity of gene expression. *PNAS* **106**, 5123–5128. arXiv:  
747 [arXiv:1408.1149](https://arxiv.org/abs/1408.1149) (2009).
- 748 59. Huang, H.-H., Qian, Y. & Del Vecchio, D. A quasi-integral controller for adaptation of genetic modules to  
749 variable ribosome demand. *Nature Communications* **9**, 5415 (2018).
- 750 60. Aoki, S. K. *et al.* A universal rationally-designed biomolecular integral feedback controller for robust perfect  
751 adaptation. *Nature* **570**, 533–537 (2019).
- 752 61. Ng, A. H. *et al.* Modular and tunable biological feedback control using a de novo protein switch. *Nature* **572**,  
753 265–269 (2019).
- 754 62. Szymczak, A. L. *et al.* Correction of multi-gene deficiency in vivo using a single 'self-cleaving' 2A  
755 peptide-based retroviral vector. *Nature Biotechnology* **22**, 589–594 (2004).
- 756 63. Berger, S. L., Cress, W., Cress, A., Triezenberg, S. J. & Guarente, L. Selective inhibition of activated but not  
757 basal transcription by the acidic activation domain of VP16: Evidence for transcriptional adaptors. English.  
758 *Cell* **61**, 1199–1208 (June 1990).
- 759 64. Schmidl, S. R. *et al.* Rewiring bacterial two-component systems by modular DNA-binding domain swapping.  
760 *Nature Chemical Biology* **15**, 690–698 (2019).
- 761 65. Muldoon, J. J. *et al.* Model-guided design of mammalian genetic programs. *Science Advances* **7**, eabe9375  
762 (2021).
- 763 66. Samaniego, C. C., Moorman, A., Giordano, G. & Franco, E. Signaling-based neural networks for cellular  
764 computation, Preprint at <https://www.biorxiv.org/content/10.1101/2020.11.10.377077v1> (2020).
- 765 67. Cuba Samaniego, C. & Franco, E. Ultrasensitive molecular controllers for quasi-integral feedback. *Cell*  
766 *Systems* **12**, 272–288 (2021).
- 767 68. Yamamoto, K. & Ishihama, A. Transcriptional response of Escherichia coli to external zinc. *Journal of*  
768 *Bacteriology* **187**, 6333–6340 (2005).
- 769 69. Procaccini, A., Lunt, B., Szurmant, H., Hwa, T. & Weigt, M. Dissecting the specificity of protein-protein  
770 interaction in bacterial two-component signaling: Orphans and crosstalks. *PLoS ONE* **6** (2011).
- 771 70. Willett, J. W. *et al.* Specificity residues determine binding affinity for two-component signal transduction  
772 systems. *mBio* **4**, 1–11 (2013).

- 773 71. McClune, C. J., Alvarez-Buylla, A., Voigt, C. A. & Laub, M. T. Engineering orthogonal signalling pathways  
774 reveals the sparse occupancy of sequence space. *Nature* **574**, 702–706 (2019).
- 775 72. Yi, T.-M., Huang, Y., Simon, M. I. & Doyle, J. Robust perfect adaptation in bacterial chemotaxis through  
776 integral feedback control. *PNAS* **97**, 4649–4653 (Apr. 2000).
- 777 73. Groisman, E. A. Feedback Control of Two-Component Regulatory Systems. *Annual Review of Microbiology*  
778 **70**, 103–124 (2016).
- 779 74. Yeo, W. S. *et al.* Intrinsic Negative Feedback Governs Activation Surge in Two-Component Regulatory  
780 Systems. *Molecular Cell* **45**, 409–421 (2012).
- 781 75. Alon, U., Surette, M. G., Barkai, N. & Leibler, S. Robustness in bacterial chemotaxis. *Nature* **397**, 168–171  
782 (Jan. 1999).
- 783 76. Lake, D., Corrêa, S. A. L. & Müller, J. Negative feedback regulation of the ERK1/2 MAPK pathway. *Cellular*  
784 *and Molecular Life Sciences* **73**, 4397–4413 (2016).
- 785 77. Yoon, S. & Seger, R. The extracellular signal-regulated kinase: Multiple substrates regulate diverse cellular  
786 functions. *Growth Factors* **24**, 21–44 (2006).
- 787 78. McKay, M. M. & Morrison, D. K. Integrating signals from RTKs to ERK/MAPK. *Oncogene* **26**, 3113–3121  
788 (2007).
- 789 79. Caunt, C. J. & Keyse, S. M. Dual-specificity MAP kinase phosphatases (MKPs): Shaping the outcome of  
790 MAP kinase signalling. *FEBS Journal* **280**, 489–504 (2013).
- 791 80. Fritsche-Guenther, R. *et al.* Strong negative feedback from Erk to Raf confers robustness to MAPK signalling.  
792 *Molecular Systems Biology* **7**, 489 (2011).
- 793 81. Nunns, H. & Goentoro, L. Signaling pathways as linear transmitters. *eLife* **7**, 1–37 (2018).
- 794 82. Salmond, R. J., Brownlie, R. J., Morrison, V. L. & Zamoyska, R. The tyrosine phosphatase PTPN22  
795 discriminates weak self peptides from strong agonist TCR signals. *Nature Immunology* **15**, 875–883 (2014).
- 796 83. Li, Q. J. *et al.* miR-181a Is an Intrinsic Modulator of T Cell Sensitivity and Selection. *Cell* **129**, 147–161  
797 (2007).
- 798 84. Gaud, G., Lesourne, R. & Love, P. E. Regulatory mechanisms in T cell receptor signalling. *Nature Reviews*  
799 *Immunology* **18**, 485–497 (2018).
- 800 85. Rodríguez-Galán, A., Fernández-Messina, L. & Sánchez-Madrid, F. Control of immunoregulatory molecules  
801 by miRNAs in T cell activation. *Frontiers in Immunology* **9**, 2148 (2018).

- 802 86. Duportet, X. *et al.* A platform for rapid prototyping of synthetic gene networks in mammalian cells. *Nucleic*  
803 *Acids Research* **42**, 13440–13451 (Nov. 2014).
- 804 87. Sandelin, A. *et al.* Mammalian RNA polymerase II core promoters: insights from genome-wide studies.  
805 *Nature Reviews Genetics* **8**, 424–436 (2007).
- 806 88. Roy, A. L. & Singer, D. S. Core promoters in transcription: Old problem, new insights. *Trends in Biochemical*  
807 *Sciences* **40**, 165–171 (2015).
- 808 89. Haberle, V. & Stark, A. Eukaryotic core promoters and the functional basis of transcription initiation. *Nature*  
809 *Reviews Molecular Cell Biology* **19**, 621–637 (2018).
- 810 90. Ede, C., Chen, X., Lin, M. Y. & Chen, Y. Y. Quantitative Analyses of Core Promoters Enable Precise  
811 Engineering of Regulated Gene Expression in Mammalian Cells. *ACS Synthetic Biology* **5**, 395–404 (2016).
- 812 91. Ponjavic, J. *et al.* Transcriptional and structural impact of TATA-initiation site spacing in mammalian core  
813 promoters. *Genome biology* **7**, R78 (2006).
- 814 92. Gao, R., Mack, T. R. & Stock, A. M. Bacterial response regulators: versatile regulatory strategies from  
815 common domains. *Trends in Biochemical Sciences* **32**, 225–234 (2007).

816 **Figures**

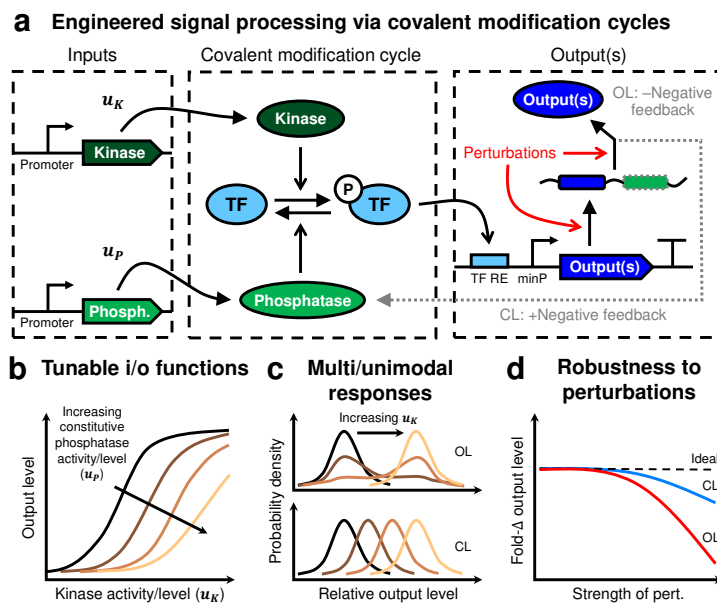


**Figure 1**



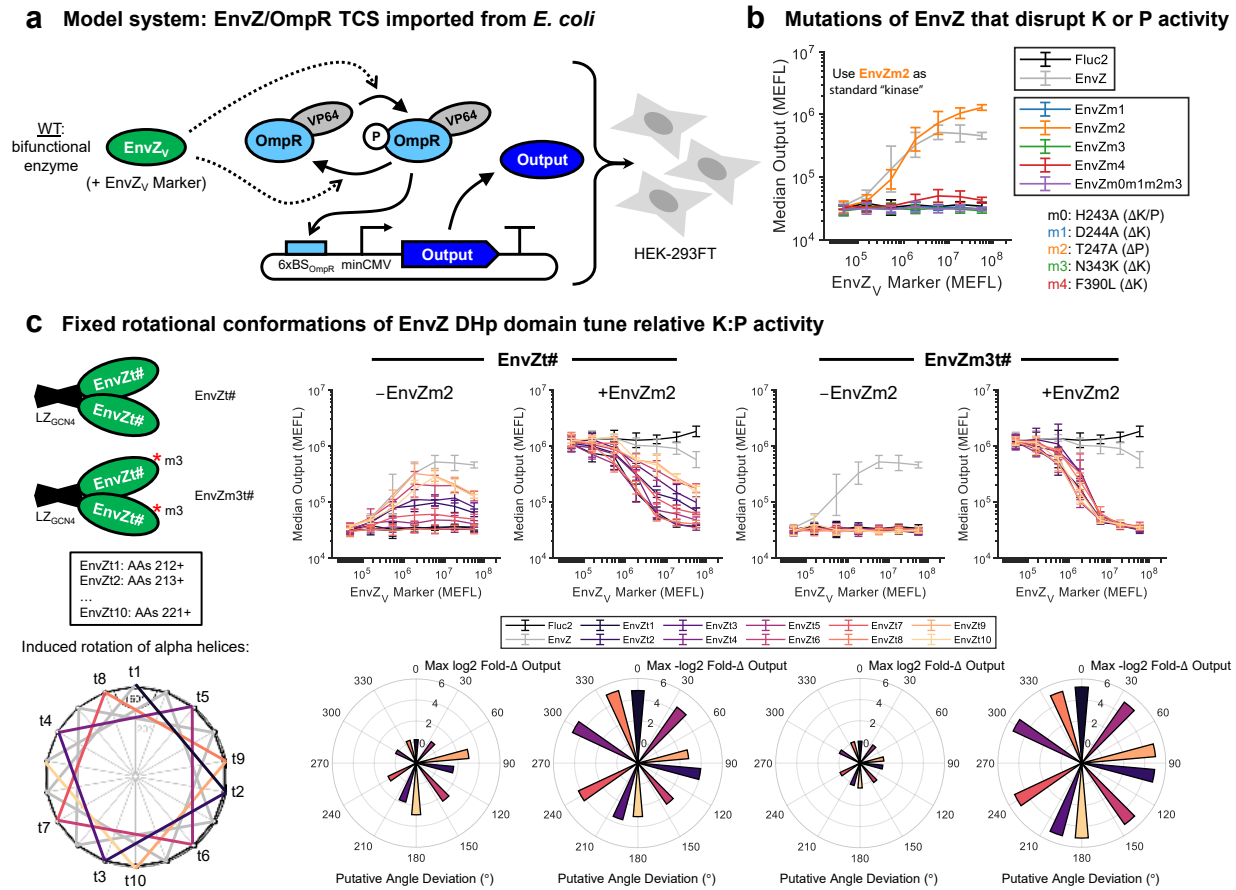
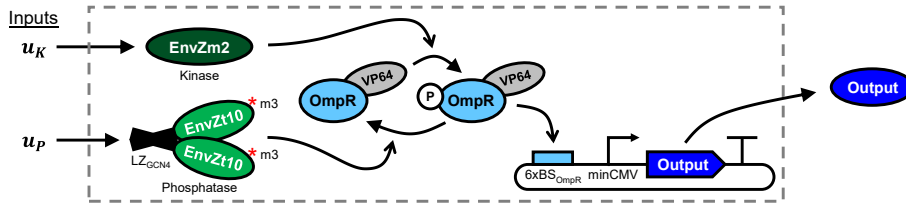
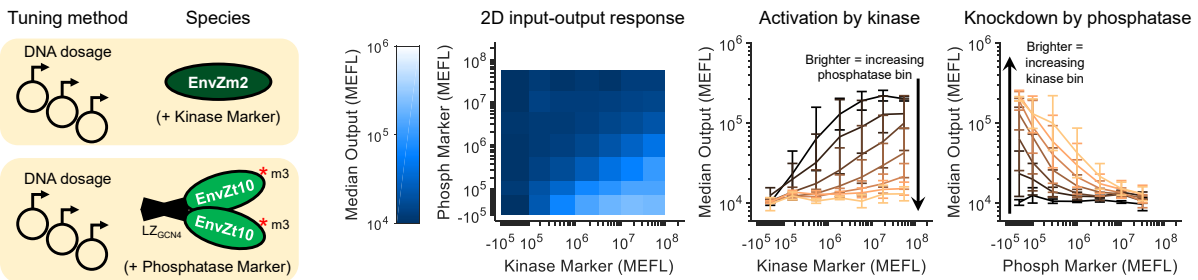


**Figure 2**

**a Tunable genetic device based on covalent modification cycles**



**b Tunable i/o responses**



**c Small molecule-tuned i/o responses**

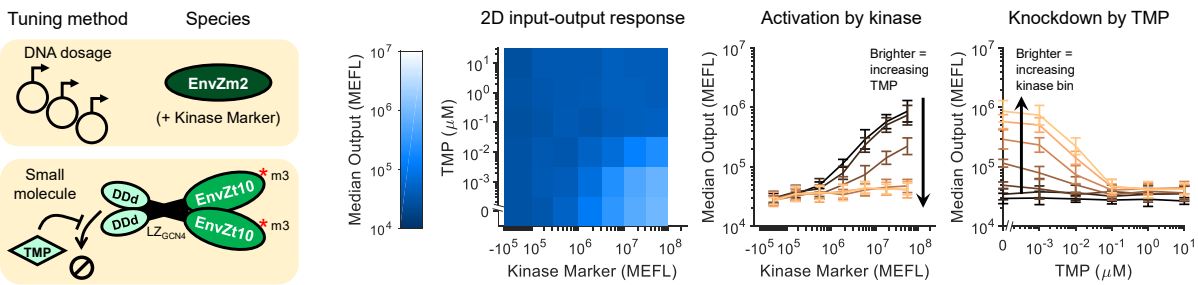


**Figure 3**

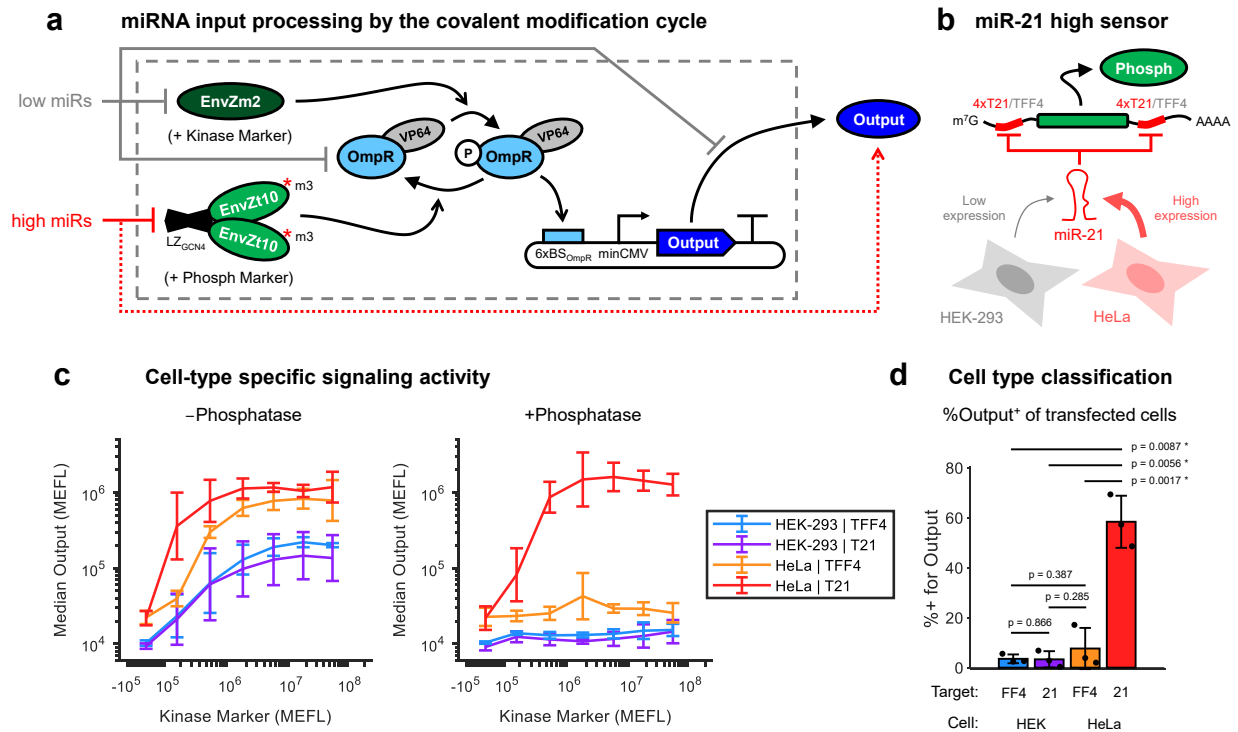
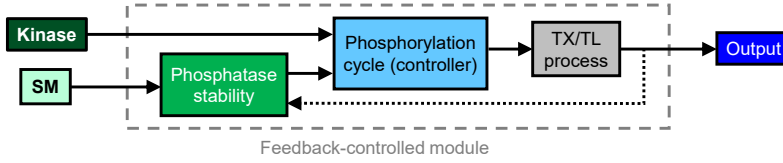
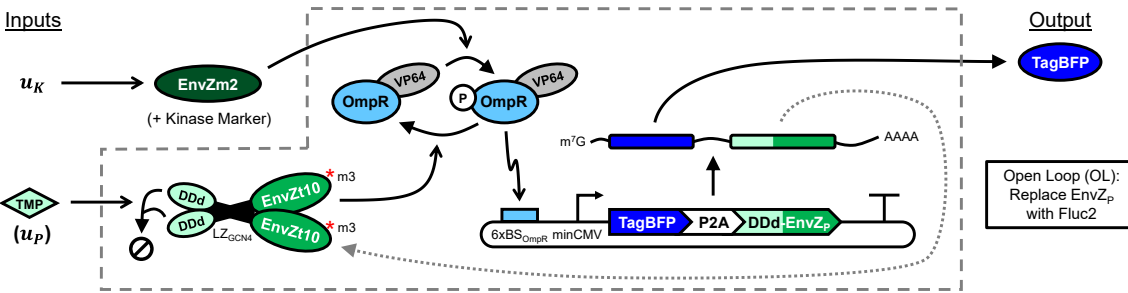


**Figure 4**

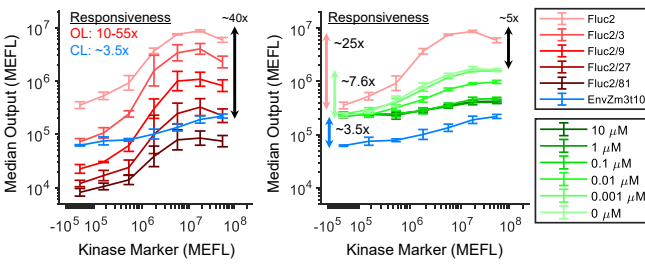
**a Phosphorylation-based feedback controller design**



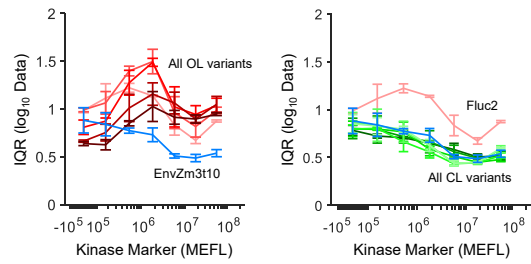
**b Feedback controller implementation**



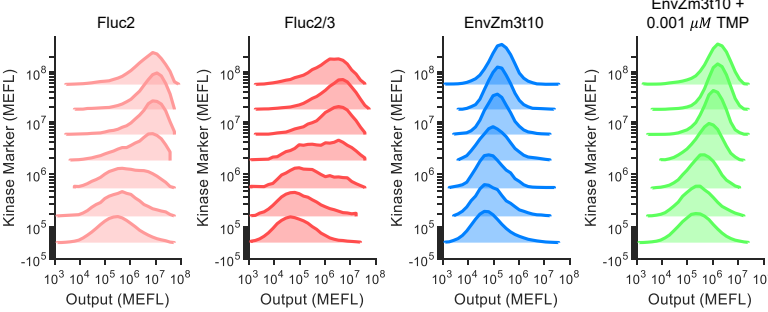
**c Kinase-output dose responses**



**d Output noise per kinase dosage**



**e Output distributions per kinase dosage**



**f Noise per level of output**

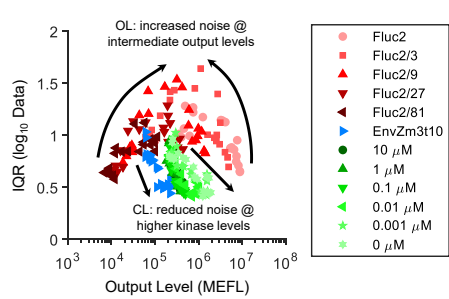
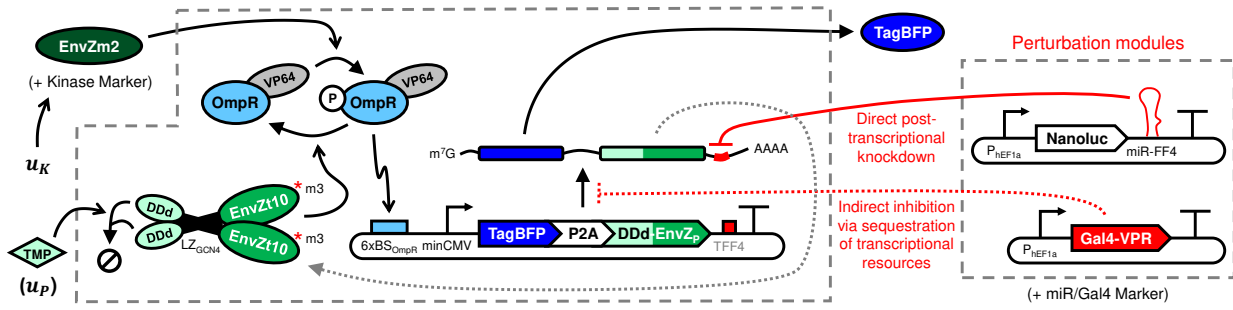
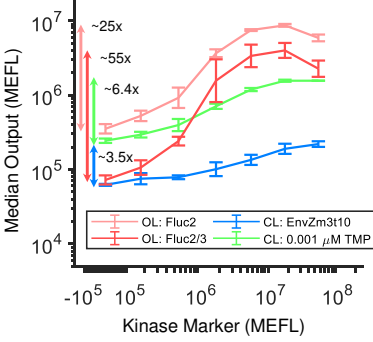


**Figure 5**

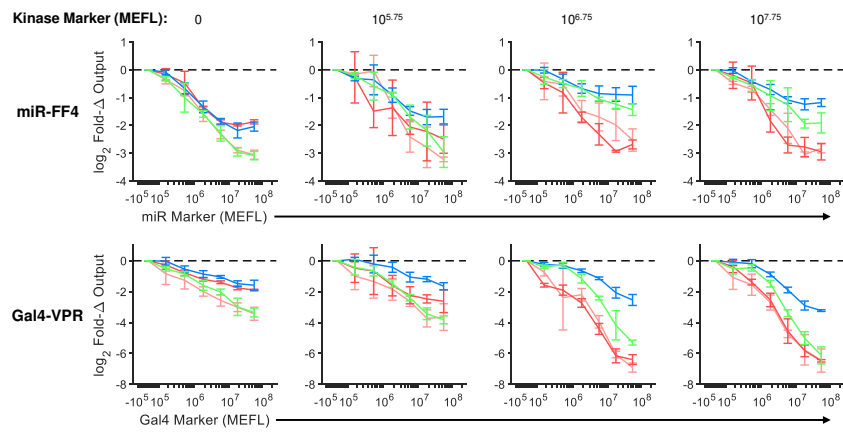
**a System for testing response of feedback controller to perturbations**



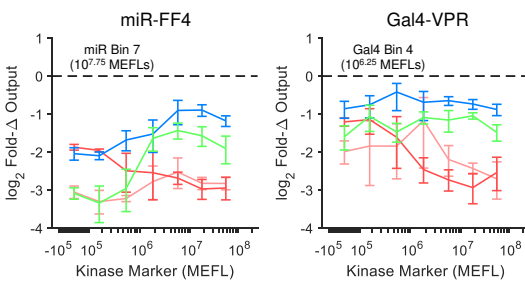
**b Kinase-output dose responses of highlighted OL and CL variants**



**c Fold-changes to perturbations**



**d Effects of perturbations per kinase level**



**e Robustness at comparable output levels**

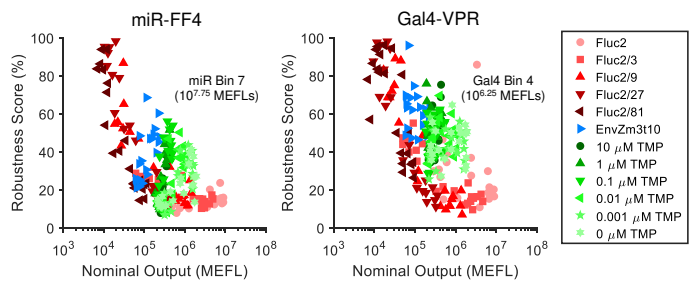


**Figure 6**

## 817 **Figure Legends**

818 **Figure 1. Overview of engineered covalent modification cycle.** (a) A covalent modification cycle (CMC) is  
819 composed of a substrate that is interconverted between an active and an inactive form by two different enzymes. Here  
820 we examine the CMC created by reversible phosphorylation/dephosphorylation of a transcription factor (TF) by a  
821 kinase and phosphatase. The inputs to this CMC,  $u_K$  and  $u_P$ , alter the production rate or catalytic rates of the kinase  
822 and phosphatase, respectively. The output(s) of the system are RNA and/or protein species produced in response to  
823 phosphorylation of the TF. Closed loop (CL) negative feedback control can be achieved by co-expressing a  
824 phosphatase with the output. Without the feedback, the expression of the outputs is open loop (OL). (b) The  
825 input/output (i/o) response of the system, *i.e.* the response of the TF-driven output(s) to kinase inputs ( $u_K$ ), can be  
826 tuned via phosphatase inputs ( $u_P$ ). (c) Negative feedback is expected to convert multimodal output responses into  
827 unimodal responses. (d) Negative feedback is expected to impart robustness to perturbations in the output production  
828 process.

829 **Figure 2. Isolation of kinase and phosphatase activity from bifunctional histidine kinases.** (a) Model system  
830 to construct a covalent modification cycle (CMC): EnvZ/OmpR proteins from *E. coli* two-component signaling  
831 (TCS). EnvZ naturally exhibits both kinase and phosphatase activities, but favors one or the other depending on its  
832 conformation. EnvZ variants (EnvZ<sub>V</sub>) are co-delivered to cells with EnvZ<sub>V</sub> Marker, a fluorescent reporter that  
833 indicates dosage per cell. (b) Evaluation of EnvZ mutants. Constitutively-expressed OmpR-VP64 (OmpR fused to  
834 the activation domain VP64) was co-transfected with a reporter plasmid comprising a promoter (P<sub>OmpR</sub>) with  
835 6xOmpR binding sites and a minimal CMV promoter driving TagBFP as the output. Each EnvZ variant (EnvZ<sub>V</sub>) was  
836 poly-transfected against the other plasmids to evaluate the EnvZ<sub>V</sub>-to-output dose-responses (see Supplementary  
837 Figure 5 for additional details). Further details about the mutants and other EnvZ variants tested are in Supplementary  
838 Figure 4. (c) Effect on EnvZ function by fixing its rotational conformation. GCN4 is fused directly to the N-terminus  
839 of EnvZ truncated between residues 212 and 221, thus connecting to the DHP domain and fixing the rotation of its  
840 alpha helices<sup>40</sup>. The top plots show the output response to each rotationally-locked variant. Samples were transfected  
841 with and without EnvZm2, which establishes a baseline of phosphorylated OmpR for testing dephosphorylation.  
842 EnvZm3t# have mutation ‘m3’ (N343K), which knocks out kinase activity. The radial plots in the bottom row  
843 indicate the maximum fold-change in output expression induced by each variant per the putative rotational  
844 conformation of the DHP domain, assuming 100° of rotation for each amino acid truncated between GCN4 and the  
845 DHP domain and setting EnvZt1 to 0°. All data were measured by flow cytometry at 48 hours post-transfection in  
846 HEK-293FT cells. All errorbars represent the mean ± s.d. of measurements from three experimental repeats.

847 **Figure 3. Tuning input/output signaling response by modulating kinase and phosphatase levels. (a)**  
848 Implementation of a covalent modification cycle with kinase (EnvZm2) and phosphatase (EnvZm3t10) variants of  
849 EnvZ. The expression level of the output can be tuned as a function of both enzymes, and inputs to each that affect  
850 their production rate ( $u_K$  and  $u_P$ ). **(b)** Tuning output expression through different dosages of kinase and phosphatase  
851 DNA. The heatmap shows the median level of output for each combination of kinase and phosphatase DNA dosages,  
852 assayed with poly-transfection<sup>44</sup> (see Supplementary Figure 18 for full data). The line plots show the same data but  
853 broken out by rows or columns. Brighter lines correspond to bins with increasing phosphatase (left) or kinase (right).  
854 **(c)** Tuning output expression through small molecule-induced degradation of the phosphatase. DDe is fused to the  
855 N-terminus of the phosphatase (see Supplementary Figure 14 for different arrangements and comparison with  
856 DDe/4-OHT). Addition of TMP stabilizes the DDe-phosphatase fusion protein<sup>45</sup>. The data is extracted from the full  
857 poly-transfection results shown in Supplementary Figures 14 & 15, selecting the middle phosphatase bin (P Marker  
858  $\approx 10^6$ ). The line plots show the same data but broken out by rows or columns. Brighter lines correspond to samples  
859 with increasing TMP concentration (left) or bins with increasing kinase (right). All data were measured by flow  
860 cytometry at 48 hours post-transfection. HEK-293 cells were used for Panel (b) and HEK-293FT for Panel (c). All  
861 errorbars represent the mean  $\pm$  s.d. of measurements from three experimental repeats. All heatmap values represent  
862 the mean of measurements from three experimental repeats.

863 **Figure 4. Cell type-specific signaling responses using covalent modification cycles. (a)** miRNA classifier  
864 design based on covalent modification cycles. miRNAs expected to be low in the target cell can be used to knock  
865 down the kinase, OmpR-VP64, and/or the output. miRNAs expected to be high in the target cell can be used to knock  
866 down the phosphatase, effectively increasing the output expression. Not shown for brevity, the level of OmpR-VP64  
867 was optimized using a feedforward controller (Supplementary Figure 16). **(b)** Design of a miR-21 sensor for  
868 classification of HeLa cells. miR-21 knocks down phosphatase levels via 4x target sites in each of its 5' and 3'  
869 untranslated regions (UTRs). As a control, a variant was made with miR-FF4 target sites (TFF4) in place of the  
870 miR-21 target sites (T21), thus preventing knockdown by miR-21. miR-21 is differentially expressed in HeLa  
871 compared to HEK-293 cells<sup>44,48</sup>. **(c)** Cell type-specific signaling responses enabled by miRNA regulation of  
872 phosphatase expression. The data is extracted from the full poly-transfection data (Supplementary Figure 18),  
873 comparing the second-highest phosphatase bin (P Marker  $\approx 10^7$ ) to the lowest (no phosphatase). **(d)** Comparison of  
874 the percent of transfected cells positive for the output for each circuit variant in HEK/HeLa cells. P-values are from  
875 two-tailed paired T-tests between each group of samples. Receiver-operator characteristic (ROC) curves are provided  
876 in Supplementary Figures 20 & 21. All data were measured by flow cytometry at 48 hours post-transfection. All  
877 errorbars represent the mean  $\pm$  s.d. of measurements from three experimental repeats.

878 **Figure 5. Design and implementation of a tunable phosphorylation-based feedback controller.** (a) Block  
879 diagram of the feedback controller design. The phosphatase acts as an output sensor, and is fed back from the output  
880 to the phosphorylation cycle. The kinase sets the reference for output expression. The output responds to inputs both  
881 to the kinase and a small molecule (SM) regulator of phosphatase stability, the latter effectively serving to tune the  
882 feedback strength. (b) Implementation of the feedback controller. the kinase is EnvZm2, the phosphatase is  
883 DDd-EnvZm3t10, and the output is the fluorescent reporter TagBFP, and the output is 2A-linked<sup>62</sup> to the phosphatase  
884 to ensure coupled transcription. Addition of TMP stabilizes DDd-EnvZm3t10 and thereby increases the feedback  
885 strength. An open loop (OL) version of the system was made by replacing the phosphatase with the luminescent  
886 protein Fluc2. Since negative feedback reduces output expression, OL variants with reduced output level were  
887 created for comparison at equivalent output levels by reducing the copy number of output reporter by fractional  
888 amounts (1:3, 1:9, 1:27, and 1:81). The kinase was poly-transfected in a separate complex to the other plasmids to  
889 measure the dose-responses of the OL and closed loop (CL) systems (see Supplementary Figures 23 for details). (c)  
890 Dose-responses of OL and CL system outputs to kinase input levels. The range of responsiveness to kinase (max fold  
891 change  $\pm$  kinase) are given for the CL and OL variants are indicated to the left of the lines. The fold-difference  
892 between max output levels for select OL and CL variants are indicated to the right of the lines. Dose-responses of the  
893 DDd-CL system are given in Supplementary Figure 28. (d) Quantification of output noise as a function of kinase  
894 input dosages. Because the output variance is log-distributed, the interquartile range (IQR) is computed on the  
895 log-transformed data. (e) Comparison of output distributions for select OL and CL variants across kinase levels. The  
896 data is representative from the first experimental repeat. All OL and CL variants are compared in Supplementary  
897 Figure 27. (f) Noise as a function of median output levels for all CL and OL variants at all kinase inputs. The  
898 individual points are drawn from all experimental repeats. All data were measured by flow cytometry at 48 hours  
899 post-transfection in HEK-293FT cells. All errorbars represent the mean  $\pm$  standard deviation of measurements from  
900 three experimental repeats.

901 **Figure 6. Mitigation of perturbations via feedback control.** (a) The CL and OL systems introduced in Figure 5  
902 were tested against two perturbations: (i) indirect transcriptional inhibition via loading of transcriptional resource by  
903 Gal4-VPR and (ii) direct post-transcriptional knockdown by miR-FF4. The kinase, perturbations, and controllers  
904 were each poly-transfected in separate DNA-lipid complexes in order to measure the 2D dose-response of the OL and  
905 CL systems to the kinase and perturbations (see Supplementary Figures 23-26 for details). (b) Dose-responses of OL  
906 and CL systems highlighted in the following panels. The Fluc2 and Fluc2/3 OL variants were chosen since they have  
907 nearly identical output levels compared to the CL with and without DDd, respectively, in the absence of kinase.  
908 Dose-responses and detailed comparisons among all OL and CL variants are provided in Supplementary Figures  
909 29-32. (c) Fold-changes (Fold- $\Delta$ s) in output expression in response to miR-FF4 (top row) and Gal4-VPR (bottom



910 row) perturbations. Each column represents an increasing amount of kinase input from left to right. The dashed lines  
911 indicate no fold-change (ideal). **(d)** Direct comparison of fold-changes to perturbations between OL and CL variants  
912 across kinase dosages. The data represents the maximum dosage of miR-FF4 (miR Marker  $\approx 10^{7.75}$  MEFLs) and a  
913 dosage of Gal4-VPR with a comparable level of knockdown to the OL (Gal4 Marker  $\approx 10^{6.25}$  MEFLs). **(f)**  
914 Robustness scores (100% – % deviation due to perturbations) for all OL and CL variants across each kinase input  
915 level at the same dosages of miR-FF4 and Gal4-VPR as highlighted in Panel (d). Nominal outputs indicate the level  
916 of output in the absence of any perturbations. The individual points are drawn from all experimental repeats. All data  
917 were measured by flow cytometry at 48 hours post-transfection in HEK-293FT cells. All errorbars represent the  
918 mean  $\pm$  standard deviation of measurements from three experimental repeats.